Histone degradation in response to DNA damage enhances chromatin dynamics and recombination rates

Hauer, Michael H.; Seeber, Andrew; Singh, Vijender; Thierry, Raphael; Sack, Ragna; Amitai, Assaf; Kryzhanovska, Mariya; Eglinger, Jan; Holcman, David; Owen-Hughes, Thomas; Gasser, Susan M.

Published in:
Nature Structural & Molecular Biology

DOI:
10.1038/nsmb.3347

Publication date:
2017

Document Version
Peer reviewed version

Histone degradation in response to DNA damage enhances chromatin dynamics and recombination rates

Michael H. Hauer[1,2], Andrew Seeber[1,2], Vijender Singh[3], Raphael Thierry[1], Ragna Sack[1], Assaf Amitai[4,+], Mariya Kryzhanovska[1], Jan Eglinger[1], David Holcman[4], Tom Owen-Hughes[3] and Susan M. Gasser[1,2,*]

Institutions

1) Friedrich Miescher Institute for Biomedical Research, Maulbeerstr. 66, CH-4058 Basel, Switzerland
2) University of Basel, Faculty of Natural Sciences, CH-4056 Basel, Switzerland
3) Centre for Gene Regulation and Expression, School of Life Sciences, University of Dundee, Dundee DD1 5EH, UK
4) Institut de Biologie de l'École Normale Supérieure, Ecole Normale Supérieure, 46 rue d'Ulm 75005 Paris, France

Present addresses

+ Institute for Medical Engineering & Science, The Massachusetts Institute of Technology, Cambridge, Massachusetts

Corresponding author statement

*Correspondence should be addressed to S.M.G.: susan.gasser@fmi.ch

Abstract

Nucleosomes are essential for proper chromatin organization and the maintenance of genome integrity. Histones are post-translationally modified and often evicted at sites of DNA breaks, facilitating recruitment of repair factors. Whether such chromatin changes are localized or genome-wide is debated. Here we show that cellular levels of histones drop 20-40% in response to DNA damage. This histone-loss occurs from chromatin, is proteasome mediated and requires both the DNA damage checkpoint and INO80 nucleosome remodeler. Histone level reduction was confirmed by SILAC-based mass spectroscopy, genome-wide nucleosome mapping and fluorescence microscopy. Chromatin decompaction and increased fiber flexibility accompany histone degradation, both in response to DNA damage and upon artificially reducing histone levels. As a result, recombination rates and DNA repair focus turnover are enhanced. Thus, we propose that a generalized reduction in nucleosome occupancy is an integral part of the DNA damage response, providing mechanisms for enhanced chromatin mobility and homology search.

-------- 150 words ---------

50 **Introduction**

51 The genomic DNA of eukaryotes is highly organized and packed into chromatin. The most basic unit of
52 chromatin is the nucleosome which is formed by 146 base base pairs of DNA that wrap around an
53 octameric core of histone proteins. Chromatin remodelers use the energy from ATP hydrolysis to change
54 the local state of chromatin by sliding/spacing or ejecting nucleosomes. These actions regulate gene
55 transcription[1], replication[2], chromatin structure and DNA repair genome-wide[3,4]. Cellular genomes are
56 constantly exposed to different sources of DNA damage, requiring that the repair machinery both
57 disrupts and restores chromatin structure[5]. Heterochromatic chromatin tends to obstruct repair protein
58 access and DNA double-strand breaks (DSB) found in heterochromatin relocate to the edge of such
59 domains[6-8], a phenomenon that requires a certain degree of physical mobility.

60 In budding yeast and human cells exposed to DNA damage, increases in chromatin mobility
61 were observed both at lesions[9-11] and at undamaged sites where no DSB could be detected[10,12]. The
62 chromatin remodeler INO80-C and activation of the DNA damage checkpoint (DDC) were implicated
63 in both processes[9,10,12]. Functionally, enhanced local DSB mobility correlated with efficient repair by
64 homologous recombination (HR)[9]. Modelling algorithms (Amitai A., Seeber A. *et al.*, ***in preparation***)
65 suggest that mobility could enhance the search for the donor sequence required for homology-based
66 repair. Consistently, elevated chromatin mobility was shown to result in genomic translocations in
67 human cells[11]. However, the mechanisms that underlie enhanced chromatin mobility have remained
68 elusive. Here we show that nucleosome degradation triggered by remodelers and checkpoint proteins
69 enhances chromatin movement and accessibility, and promotes efficient repair.

70

71

72

73

74

75

76 **Results**

77 **DNA damage triggers extensive histone loss from chromatin**

78 To investigate whether DNA damage and DDC activation affect chromatin structure and/or composition
79 genome-wide, we used quantitative SILAC mass spectrometry in *Saccharomyces cerevisiae* and
80 measured histone abundance before and after acute treatment (1 hour) with the radiomimetic drug
81 Zeocin. Relative ratios of non-modified histone peptides (damage over control - L/H) indicate a
82 substantial loss of 20±6 % of all core histones H2A, H2B, H3 and H4 (**Fig. 1a**, **Supplementary Fig.**
83 **1a-f**). Interestingly, levels of the histone variant Htz1 (H2A.Z) remained rather stable. Quantitative
84 immunoblot analysis confirmed our observations and showed robust DDC activation (γH2A signal,
85 Rad53 upshift) along with a dose-dependent relationship between histone H3/H4 loss and Zeocin
86 treatment (**Fig. 1b**). The same effect was observed using another source of DNA damage, ionizing
87 radiation (γ-IR) (**Supplementary Fig. 2a-d**).

88 Despite being highly quantitative for protein abundance, mass spectrometry data does not
89 distinguish between histone pools and nucleosomes, and it lacks positional information. To investigate
90 whether entire nucleosomes were lost globally following DNA damage or at specific genomic loci, we
91 performed genome-wide nucleosome mapping. First, we found that the positioning of nucleosomes
92 around the promoters of yeast genes changed little following damage induction (**Fig. 1c**). To assess
93 global changes in nucleosome abundance, we implemented internal standardization by mixing defined
94 numbers of *Candida glabrata* cells with the experimental *Saccharomyces cerevisiae* cells prior to
95 chromatin preparations[13]. Normalization of the *S. cerevisiae* reads with respect to the *C. glabrata* reads
96 showed that there was a drop in nucleosome occupancy both within promoters and across coding regions
97 following Zeocin treatment (**Fig. 1c and Supplementary Table 1)**. This effect was just as strong on a
98 subset of 750 low expression genes (**Fig. 1c**) as on highly transcribed genes (**Supplementary Fig. 2e**),
99 suggesting that transcription is unlikely to regulate or drive the reduction. Finally, we found no
100 preferential depletion specific structural elements such as centromeres or telomeres, arguing that the
101 effect is widespread.

102 To determine the kinetics of histone reduction, we used time-lapse live cell tracking of
103 functional fluorescently labeled ectopic histone H2B (H2B-CFP) or control Htz1-mEos and Nup49-
104 GFP, which labels the nuclear rim (**Fig. 1d**, **Supplementary Fig. 2g**, **Supplementary Video 1**). We
105 used microfluidic chambers to trap cells and pulse-treated them for 1h with Zeocin, generating roughly
106 4-7 DSBs per genome[14]. Histone H2B degradation (20±1.7% compared to undamaged cells) occurred
107 within 30 minutes of Zeocin exposure. Neither Nup49-GFP (**Supplementary Fig. 2f**) nor the Htz1-
108 mEos control showed differential loss following DNA damage, suggesting that the induced histone
109 degradation only targets core histones (**Fig. 1d**). Combined with our mass-spectroscopy and immunoblot
110 data, these results suggested a rapid degradation of histones, rather than simply eviction from chromatin.
111 Earlier, Gunjan *et al.* had shown that an excess of nonchromatin-bound histones is phosphorylated by
112 the Rad53 checkpoint kinase, and then subsequently ubiquitinated and subject to proteasomal
113 degradation[15,16]. This prompted us to test whether the proteasome inhibitor MG132 or mutation of the
114 26S proteasome (*pre1-1, pre2-2*)[17] would suppress the loss of histones from chromatin. Consistent with
115 proteasome involvement, both the inhibitor and the mutations in *PRE1* and *PRE2* genes suppressed the
116 DNA damage-induced H3 or H4 degradation (**Fig. 2**). Moreover, by synchronizing cells in G1, or
117 releasing them into S phase prior to damage, we found that degradation occurs in both phases of the cell
118 cycle (**Supplementary Fig. 3**).

119 We considered that the observed histone loss might be accentuated by impaired expression of
120 histone genes, which are tightly regulated and show promoter-dependent upregulation in S phase. To
121 eliminate this confounding factor, we placed the H3 and H4 genes under the control of the galactose
122 promoter in a strain in which both endogenous H3 and H4 copies were deleted (histone-shutdown strain,
123 **Supplementary Fig. 4a**). With constitutive H3/H4 expression (growth in media with low level
124 galactose), we found the same depletion effect following exposure to Zeocin as in cells with endogenous
125 histone genes, arguing that DNA damage induces an active degradation of histones, and not simply a
126 loss of new histone synthesis (**Supplementary Fig. 4**). The loss of histones is rapid and so substantial
127 that by 1h, every third nucleosome could be removed from DNA. It is therefore likely that higher-order
128 chromatin structure changes in response to DNA damage.

129

130 **Damaged chromatin increases mobility, decompaction and flexibility**

131 The increase in chromatin movement following DNA damage has been well documented, although the
132 mechanisms leading to enhanced mobility remained elusive[12,18,19]. To see if histone loss might be at the
133 root of this phenomenon, we examined the physical characteristics of yeast chromatin under the same
134 conditions that triggered histone loss. Using improved imaging protocols, we monitored the volume of
135 chromatin domains in three-dimensional (3D) space, the inherent flexibility of the nucleosome polymer
136 and the physical movement of fluorescently tagged sites.

137 Previous studies in which chromatin mobility was quantified used low sampling rates during
138 live cell imaging (Δt=1.5 sec) to determine the trajectory of a moving locus and the area explored (radius
139 of constraint)[9-12,20]. However, such low time-resolved data yields little information on chromatin fiber
140 compaction or flexibility. To resolve this, we used a novel high-speed imaging technique (300 ms or 80
141 ms imaging intervals) with which we first confirmed that increased chromatin mobility can be monitored
142 at a non-damaged site (*MET10*) in cells responding to widespread DNA damage (**Fig. 3a,**
143 **Supplementary Fig. 5a**). By applying an analysis based on polymer models to our high-speed imaging
144 data (Amitai A., Seeber A. *et al.,* ***in preparation***), we estimated biophysical parameters that predict both
145 the expansion of chromatin (reflected by an increase in the anomalous exponent α) and the loss of
146 constraining forces that limit chromatin movement (as seen by decrease in the spring constant K_C) (**Fig.**
147 **3b and Supplementary Fig. 5b**).

148 To examine whether the 3D volume of a defined chromatin domain was altered within the
149 nucleus, we used super-resolution microscopy coupled with subsequent machine-learning and 3D pixel
150 classification analysis. Using this technique, we measured the change in volume of TetR-mCherry
151 tagged chromosomal loci (chromatin expansion) in cells fixed 30 min after exposure to different
152 amounts of Zeocin (**Fig. 3c**). Indeed, we scored a dose-dependent decompaction of S phase chromatin:
153 3D TetR-mCherry foci volumes expanded with increased amounts of damage (**Fig. 3d**).

154 The second prediction from the polymer modeling of locus dynamics was that the flexibility of
155 the chromatin fiber would be enhanced after DNA damage. Thus, we monitored chromatin flexibility
156 with confocal microscopy and measured the 3D distances between two differentially labeled genomic

157 loci positioned on the same chromosome arm. We used two independent sets of loci spaced at genomic
158 distances of either 320 kbp on Chr XIV or 50 kbp on Chr III. For the first set, we synchronized cells,
159 fixed them before or after Zeocin treatment and calculated the average of all distances measured between
160 the lacI-GFP and TetR-mRFP fluorescently tagged loci (**Fig. 4a**). We find that after DNA damage, the
161 average inter-spot distance increases significantly both in G1- (0.97-1.2 μm) and S-phase cells (0.99-
162 1.12μm). For the second set of data, a similar approach was taken but we measured the inter-distance
163 between CFP-lacI and TetR-mRFP tagged foci on Chr III in real time (**Supplementary Video 2**). In all
164 cases we included Rad52-GFP and ensured that there was no overlap of Rad52-GFP with either of the
165 other two fluorescent signals, assuring that the measured changes do not arise from effects linked to
166 local DNA repair events. Analysis of relative mean squared distance changes and the average of all
167 measured inter-distances reveals a robust increase in inter-spot dynamics and distances following Zeocin
168 treatment (**Fig. 4b**). These data are consistent with a model in which damage-triggered histone
169 degradation reduces the amount of nucleosomal constraints within the chromatin fiber, causing
170 chromatin to expand. The enhanced physical dynamics would be a reflection of increased flexibility.

171 **Histone abundance dictates chromatin movement and decompaction**

172 To confirm that increased chromatin mobility and decompaction arise as a consequence of histone loss,
173 we made use of a histone-shutdown strain that expresses H3 and H4 under the control of the *GAL1-10*
174 promoter which is susceptible to media-controlled repression as well as induction (**Fig. 5a**). After 1h in
175 galactose, we released α-factor arrested cells bearing this shutdown construct into raffinose-containing
176 medium. Depending on the concentration of raffinose, we observed reduced *GAL1-10*-driven
177 expression, lowering histone levels in a controlled manner by 39% within an hour (**Supplementary Fig.
178 6ab**). This artificial reduction of histones did not cause DNA damage checkpoint activation, even when
179 levels were reduced extensively (**Supplementary Fig. 6b**). Using the appropriate galactose:raffinose
180 mixture, however, we could reduce histone levels in a controlled manner, even in the absence of damage
181 (**Fig. 5b)**, after which we monitored both chromatin decompaction (**Fig. 5c**) and a striking increase of
182 chromatin mobility, measured at the *MGS1* locus after 1h on the defined medium (**Fig. 5d**).

183 To further validate these findings, we made use of a mutant bearing deletions of both high-
184 mobility group protein one (HMGB1) orthologues *NHP6A* and *NHP6B* (*nhp6a*Δ*nhp6b*Δ, for simplicity

185 called *nhp6*Δ), which was previously described as having reduced levels of core histone proteins[21]. Here,
186 we show that *nhp6*Δ does not trigger endogenous damage checkpoints, and has neither an altered FACS
187 distribution (**Fig. 6b**) nor Rad53 activation (**Supplementary Fig. 7a**), yet by tracking chromatin
188 mobility with the high-speed imaging regime we find that the mobility of two labeled foci, *MET10* and
189 *PES4*, is significantly enhanced in *nhp6*Δ cells (**Fig. 6cd, Supplementary Fig. 7b**). High resolution
190 time-lapse imaging of the GFP-LacI-tagged *PES4* or the TetR-mCherry-tagged *MET10* locus further
191 confirms an increase in chromatin flexibility which is reflected by a decrease in the spring constant K_C,
192 and a positive trend in the anomalous exponent α (**Fig. 6e, Supplementary Fig. 7cd**). Finally, using
193 super-resolution microscopy we monitored an increase in 3D volume of the TetR-mCherry labeled
194 *MET10* locus in *nhp6*Δ cells, which was more pronounced in an asynchronous culture, for unknown
195 reasons (**Fig. 6f**). Combined with the effects observed in the histone shutdown strain, these
196 manipulations argue for a direct link between histone levels and chromatin movement.

197 **Histone loss is checkpoint and INO80-C dependent and modulates recombination efficiency**

198 DNA damage activates the central DDC kinase Mec1 (ATR) which initiates a widespread
199 phosphorylation cascade leading to a global damage response and cell-cycle arrest. Additionally, repair
200 proteins such as Mre11, Exo1, Rad51 and Rad52 act locally on DNA to mediate resection and
201 preparation for either repair by homologous recombination or end-joining. Among Mec1 targets are the
202 downstream effector kinase Rad53 (CHK2)[22] and multiple subunits of the INO80-C remodeler[23,24]. Since
203 both INO80-C and DDC proteins were implicated in a general increase in chromatin mobility in
204 response to DNA damage[12], we hypothesized that these factors may also regulate histone loss, which
205 we find can trigger enhanced chromatin mobility.

206 Using immunoblotting, we found that strains lacking checkpoint kinases Mec1 or Rad53
207 completely abolished histone degradation after Zeocin treatment (**Fig. 7ab**). More strikingly, the same
208 dependency was observed for strains deleted for INO80-C subunits Arp8, Ies4 or Arp5 which do not
209 participate in the DDC, but remodel nucleosomes (**Fig. 7ab**). Importantly, histone loss occurred
210 independently of Rad51 and Exo1 showing that local repair events are not necessary for the DDC-
211 triggered degradation of histones. We further confirmed this with two other assays: H2B-CFP
212 fluorescence monitoring over time (**Fig. 7c**) and super-resolution microscopy of tagged locus 3D

213 volumes (**Fig. 7d**). In all cases we find that histone loss and chromatin expansion required the Mec1-
214 mediated checkpoint and intact INO80-C: no histone loss or chromatin expansion is seen in *mec1*Δ*sml1*Δ
215 and *rad53*Δ nor in *arp8*Δ), while cells bearing *sml1*Δ (a control for the *mec1*Δ*sml1*Δ) and *rad51*Δ
216 behaved like their wild-type counterparts in response to damage (**Fig. 7c-d**).

217 The main role of the DDC kinase Mec1/ATR is to trigger a cell-wide stress response that helps
218 the cell cope with DNA damage. This appears to be, at least in part, mediated by the remodeler INO80-
219 C[23,24]. The importance of chromatin-remodeling in histone degradation, is not entirely surprising, given
220 that Ino80 was recently shown to interact with Cdc48, an AAA^+ ATPase involved in proteasome-
221 dependent protein degradation[25]. Moreover, both Mec1 and INO80-C are linked to RNA Pol II eviction
222 at sites of replication fork-transcription collision[24]. Thus, these genetic dependencies further validate our
223 model that histone degradation and chromatin expansion are the key phenomena underlying damage-
224 enhanced chromatin movement (**Fig. 7e**). Our data further suggest that a failure to degrade histones
225 might impair the access of repair proteins to chromatin, giving an explanation for previously observed
226 repair deficiencies in these mutants[26,27].

227 To examine the functional relevance of the observed reduction in nucleosome occupancy
228 triggered by DNA damage, and to test the hypothesis that nucleosome reduction facilitates homologous
229 recombination and thus DNA repair, we made use of a recombination assay that monitors the integration
230 rates of two different *URA3* cassettes (800 bp homology or 82 bp homology) at two independent loci
231 (*MGS1* and *URA3*). In otherwise isogenic haploid strains, we impaired INO80-C activity by disrupting
232 its nucleosome-binding subunit Arp8 (*arp8*Δ) or deleted both *NHP6* genes, to reduce nucleosome levels
233 genome-wide[21]. Consistent with previously reported recombination defects in *arp8*Δ[26,27], we see reduced
234 recombination rates in this mutant, while rates were significantly increased in the *nhp6*Δ strain (**Fig.
235 8a**). Interestingly, Liang *et al.* had shown that deletion of the histone H3-H4 gene copy 2 (HHT2-HHF2)
236 can confer resistance to DNA damaging agents and restore the viability of DDC mutants under stress
237 conditions[16]. Thus, we hypothesized that artificially lowering histone levels by Nhp6 removal might
238 rescue *arp8*Δ sensitivity and even increase the fitness of wild-type cells under damaging conditions.
239 Using a recovery assay that scores cell survival after a 1h treatment with increasing amounts of Zeocin,
240 we found that *nhp6*Δ cells recover better from acute DNA damage than a wild-type strain, and that

241 lowering nucleosome occupancy by deleting *NHP6* partially rescues the Zeocin sensitivity of an *arp8*Δ
242 strain (**Fig. 8b**).

243 The observation that increased recombination rates in *nhp6*Δ cells stem from changes in
244 nucleosome occupancy, prompted us to test whether gene targeting rates could also be increased by
245 other approaches that reduce histone levels. Hence, we used the same recombination assay in our
246 histone-shutdown strain and followed the integration of two different hygromycin-resistance markers
247 either at *ATG2* or *MGS1*. This was done directly after a 2h incubation in raffinose-containing medium
248 (raffinose only or a defined 1:20 galactose:raffinose mixture) which reduces histone H3 and H4 levels
249 (**Fig. 8c**). Consistent with the *nhp6*Δ experiment, we found that a reduction of histone levels by means
250 of transcriptional repression significantly enhances the integration rates of both *ATG2::hygro* and
251 *MGS1::hygro* PCR products (**Fig. 8d**).

252 Finally, we used fluorescence microscopy to follow the kinetics of Rad52-GFP focus formation
253 and dissolution during 16h after a brief exposure to Zeocin. We find fewer Rad52 (BRCA2) foci in
254 *nhp6*Δ *vs* wild-type cells (**Supplementary Fig. 7e**). Since Rad52 accumulates at sites of damage and
255 disappears upon completion of recombination mediated repair[28], this result suggests that a reduction in
256 histone levels enhances the turnover of the recombination-mediated repair reaction.

257 **Discussion**

258 In a robust combinatorial approach, we used quantitative mass spectrometry, fluorescent live cell
259 microscopy and genome-wide nucleosome mapping to show that core histone proteins but not histone
260 variant Htz1 are degraded from chromatin when the genome is challenged with DNA damage. This
261 requires checkpoint activation, INO80-C function and is mediated through the proteasome. Furthermore,
262 reducing the levels of histones on DNA enhances chromatin mobility, decompaction and fiber
263 flexibility. Proteins that function uniquely in recombination-mediated DNA repair (Rad51, Exo1) were
264 not involved in histone loss, while the Mec1-target INO80-C, a chromatin remodeler implicated in
265 efficient repair, is. Other studies have postulated a release of chromosomal tethers around the centromere
266 as the source for altered chromatin mobility[20,29]. This, however, is unable to account for the observed

267 expansion of non-centromeric chromatin nor for the observed dependence on INO80-C for these events.
268 Furthermore, there is no evidence to date that centromeres delocalize in response to damage.

269 While we cannot rule out that other mechanisms also contribute to nuclear or chromosomal
270 motion, our data irrefutably demonstrate that a reduction of histone levels, even in the absence of DNA
271 damage, is sufficient to decompact chromatin and enhance chromatin mobility. We suggest that histone
272 degradation facilitates the search for donor sequences, an event required for DSB repair by homologous
273 recombination with a non-sister template, and that chromatin decompaction might further enhance the
274 access of DNA (both damage and template) to the repair machinery. On the other hand, mobility might
275 also help disrupt improper pairing events during HR. Recombination assays indicate that a reduction in
276 nucleosome occupancy by *NHP6* deletion cells or by means of transcriptional histone gene repression
277 increases gene targeting rates and enhances the turnover rate of repair processes. While controlled
278 histone loss might facilitate repair, its misregulation and the resulting effects in chromatin structure and
279 dynamics are likely to promote oncogenic translocations that might drive tumorigenesis.

280 Taken together, our study identifies histone loss as a fairly immediate response to DNA damage
281 checkpoint activation and implicates remodeler-dependent histone degradation as a novel and integral
282 part of the DNA damage response. We demonstrate how changes in chromatin composition can affect
283 the physical characteristics of chromatin and we show that artificial histone level reduction can be used
284 to increase recombination efficiency. To understand how the posttranslational modification status of
285 histones and the entire chromatin proteome changes upon DNA damage requires further investigation.
286 We speculate that gene targeting rates in mammalian cells can also be improved by manipulating histone
287 occupancy.

288

289

290

291

Acknowledgements

M.H.H. thanks Shany Koren-Hauer for critical reading and assistance in preparing the manuscript and Vincent Dion and Helder Ferreira for fruitful discussions and advice. We thank Vincent Dion (strain GA-5816), James Haber (strain JKM-179); Brian Luke (strain GA-3364), Kerstin Bystricky (precursor strain for GA-9777, strain GA-9227), Jean-Marc Galan (strain GA-1364, GA-1365, GA-1366) and Fred Winston (plasmids #3494, #3495) for reagents and material. We are grateful for the technical assistance provided by Laurent Gelman (microscopy), Steven Bourke (microscopy) and Hubertus Kohler (FACS). M.H.H. thanks the Bioinformatics facility for help in getting started with R. We thank all members of the FMI Protein Analysis and Microscopy facilities for valuable advice and support. We thank all members from the Gasser laboratory for valuable discussions and technical support. M.H.H. was supported by a PhD fellowship of the Boehringer Ingelheim Fonds. S.M.G. thanks the HFSP, SNSF and the Novartis Research Foundation for support.

Author contributions

M.H.H. and S.M.G wrote the manuscript. M.H.H. designed experiments and analyzed the data. M.H.H. performed most of the experiments. A.S. contributed to experimental design, data analysis, the manuscript and performed high-speed live cell tracking upon Zeocin treatment. M.H.H. planned and M.H.H. and A.S. performed the ectopic integration assays and the Rad52-YFP recovery assay. M.K. assisted in ectopic recombination assays. V.S. and T.O.-H. performed and analyzed genome-wide nucleosome mapping. A.A. and D.H. performed biophysical analysis of high-speed tracking data. R.T. performed and maintained the coding for 3D SIM-data analysis. R.S. performed all mass spectrometry measurements and the analysis of label-free experiments. J.E. performed and maintained the coding of tools for 3D inter-distance measurements. All the authors discussed the data and participated in the preparation of the manuscript.

Competing Financial Interests

The authors declare no competing financial interests.

References (main text only)

1. Boettiger, A.N. et al. Super-resolution imaging reveals distinct chromatin folding for different epigenetic states. *Nature* **529**, 418-22 (2016).
2. Aze, A., Sannino, V., Soffientini, P., Bachi, A. & Costanzo, V. Centromeric DNA replication reconstitution reveals DNA loops and ATR checkpoint suppression. *Nat Cell Biol* **18**, 684-91 (2016).
3. Gerhold, C.B., Hauer, M.H. & Gasser, S.M. INO80-C and SWR-C: guardians of the genome. *J Mol Biol* **427**, 637-51 (2015).
4. Seeber, A., Hauer, M. & Gasser, S.M. Nucleosome remodelers in double-strand break repair. *Curr Opin Genet Dev* **23**, 174-84 (2013).
5. Soria, G., Polo, S.E. & Almouzni, G. Prime, repair, restore: the active role of chromatin in the DNA damage response. *Mol Cell* **46**, 722-34 (2012).
6. Chiolo, I. et al. Double-Strand Breaks in Heterochromatin Move Outside of a Dynamic HP1a Domain to Complete Recombinational Repair. *Cell* **144**, 732-744 (2011).
7. Lemaitre, C. et al. Nuclear position dictates DNA repair pathway choice. *Genes Dev* **28**, 2450-63 (2014).
8. Torres-Rosell, J. et al. The Smc5-Smc6 complex and SUMO modification of Rad52 regulates recombinational repair at the ribosomal gene locus. *Nat Cell Biol* **9**, 923-31 (2007).
9. Dion, V., Kalck, V., Horigome, C., Towbin, B.D. & Gasser, S.M. Increased mobility of double-strand breaks requires Mec1, Rad9 and the homologous recombination machinery. *Nat Cell Biol* **14**, 502-9 (2012).
10. Mine-Hattab, J. & Rothstein, R. Increased chromosome mobility facilitates homology search during recombination. *Nat Cell Biol* **14**, 510-7 (2012).
11. Roukos, V. et al. Spatial dynamics of chromosome translocations in living cells. *Science* **341**, 660-4 (2013).
12. Seeber, A., Dion, V. & Gasser, S.M. Checkpoint kinases and the INO80 nucleosome remodeling complex enhance global chromatin mobility in response to DNA damage. *Genes Dev* **27**, 1999-2008 (2013).
13. Hu, B. et al. Biological chromodynamics: a general method for measuring protein occupancy across the genome by calibrating ChIP-seq. *Nucleic Acids Res* **43**, e132 (2015).
14. Povirk, L.F., Wubter, W., Kohnlein, W. & Hutchinson, F. DNA double-strand breaks and alkali-labile bonds produced by bleomycin. *Nucleic Acids Res* **4**, 3573-80 (1977).
15. Gunjan, A. & Verreault, A. A Rad53 kinase-dependent surveillance mechanism that regulates histone protein levels in S. cerevisiae. *Cell* **115**, 537-49 (2003).
16. Liang, D., Burkhart, S.L., Singh, R.K., Kabbaj, M.H. & Gunjan, A. Histone dosage regulates DNA damage sensitivity in a checkpoint-independent manner by the homologous recombination pathway. *Nucleic Acids Res* **40**, 9604-20 (2012).

358 17. Heinemeyer, W., Kleinschmidt, J.A., Saidowsky, J., Escher, C. & Wolf, D.H. Proteinase yscE,
359 the yeast proteasome/multicatalytic-multifunctional proteinase: mutants unravel its function in
360 stress induced proteolysis and uncover its necessity for cell survival. *EMBO J* **10**, 555-62
361 (1991).

362 18. Dion, V. & Gasser, S.M. Chromatin movement in the maintenance of genome stability. *Cell*
363 **152**, 1355-64 (2013).

364 19. Krawczyk, P.M. et al. Chromatin mobility is increased at sites of DNA double-strand breaks.
365 *Journal of Cell Science* **125**, 2127-2133 (2012).

366 20. Strecker, J. et al. DNA damage signalling targets the kinetochore to promote chromatin
367 mobility. *Nat Cell Biol* **18**, 281-90 (2016).

368 21. Celona, B. et al. Substantial histone reduction modulates genomewide nucleosomal occupancy
369 and global transcriptional output. *PLoS Biol* **9**, e1001086 (2011).

370 22. Sanchez, Y. et al. Regulation of RAD53 by the ATM-like kinases MEC1 and TEL1 in yeast cell
371 cycle checkpoint pathways. *Science* **271**, 357-60 (1996).

372 23. Morrison, A.J. et al. Mec1/Tel1 phosphorylation of the INO80 chromatin remodeling complex
373 influences DNA damage checkpoint responses. *Cell* **130**, 499-511 (2007).

374 24. Poli, J. et al. Mec1, INO80, and the PAF1 complex cooperate to limit transcription replication
375 conflicts through RNAPII removal during replication stress. *Genes Dev* **30**, 337-54 (2016).

376 25. Lafon, A. et al. INO80 Chromatin Remodeler Facilitates Release of RNA Polymerase II from
377 Chromatin for Ubiquitin-Mediated Proteasomal Degradation. *Mol Cell* **60**, 784-96 (2015).

378 26. Chen, X. et al. The Fun30 nucleosome remodeller promotes resection of DNA double-strand
379 break ends. *Nature* **489**, 576-80 (2012).

380 27. van Attikum, H., Fritsch, O. & Gasser, S.M. Distinct roles for SWR1 and INO80 chromatin
381 remodeling complexes at chromosomal double-strand breaks. *Embo j* **26**, 4113-25 (2007).

382 28. Lisby, M., Barlow, J.H., Burgess, R.C. & Rothstein, R. Choreography of the DNA damage
383 response: spatiotemporal relationships among checkpoint and repair proteins. *Cell* **118**, 699-713
384 (2004).

385 29. Verdaasdonk, J.S. et al. Centromere tethering confines chromosome domains. *Mol Cell* **52**, 819-
386 31 (2013).

387

388

389

390

391

392

393

394

395

396 # Figure legends

397 **Figure 1: DNA damage triggers a global loss of core histones from chromatin**

398 Damage-dependent global histone degradation quantified by (**a**) SILAC mass spectrometry on
399 chromatin fractions from two independent cells pools (for further information see **Supplementary Fig.**
400 **1**). Boxplots show light/heavy histone peptide distribution indicating the degradation of core histones
401 and, to a lesser extent, Htz1 (H2A.Z). (**b**) Right: Representative immunoblot analysis using antibodies
402 against H3 and H4 on whole cell extracts from asynchronous (asy.) wild-type cultures in response to
403 Zeocin treatment. Rad53 and γH2A were probed to confirm checkpoint activation. MCM2 was used to
404 control for loading and Ctr. represents bands on the Ponceau stained membrane. Left: Schematic
405 illustrates the experimental setup and bar graph shows mean values of immunoblot quantification of H3
406 and H4 blots from at least four independent experiments upon Zeocin treatment relative to the control
407 condition. Asterisk indicates phosphorylation-dependent Rad53 mobility shift. (**c**) Genome-wide
408 nucleosome mapping. Scheme illustrates the effect of histone loss on nucleosome reads. Graphs show
409 the distribution of nucleosome reads over all genes and over the bottom 10% of low level expressed
410 genes aligned to the TSS from four independent experiments (±s.d. is shaded). (**d**) Live single-cell
411 microscopy of H2B-CFP and Htz1-mEos. Graphs show the experimental outline, representative images
412 and the mean fluorescent signals of all individual cells (cell numbers indicated in graph) per treatment
413 over time relative to the control (Ctr.) condition. Scale bar is 2 µm. Uncropped blot images are shown
414 in **Supplementary Dataset 1**. Boxplots in **a** represent median values, interquartile ranges and whiskers.
415 Graphs in **b**,**d** show means ± s.e.m, in **c** ± s.d..

416

417 **Figure 2: Histones are degraded by the proteasome**

418 (**a**) Scheme illustrates the experimental setup. (**a-b)** Immunoblot analysis and quantification showing
419 H3 or H4 levels before and after Zeocin treatment in whole cell extracts from asynchronously (Asy.)
420 growing wild-type cells (**a**, experiment was done in triplicate) or *erg6*Δ cells (**b**, experiment was done
421 in triplicate) treated with the proteasome inhibitor MG132. MG132 permeability is increased in *erg6*Δ
422 cells which rescues histone H3 from being degraded. Antibodies against ubiquitin (Ubi) indicate proper

423 function of the MG132 inhibitor validating the experimental protocol. (**c**) Immunoblot analysis and
424 quantification showing H4 levels in response to Zeocin treatment in wild-type and 26S proteasome
425 dysfunctional cells (*pre1-1*, *pre2-2*) (experiment was done in four replicates). Mutations in *PRE1* and
426 *PRE2* suppress histone H4 degradation. Rad53 and γH2A were probed to confirm checkpoint activation.
427 Ctr. shows loading and represents bands on the original gel (UV-TGX stained). Uncropped blot images
428 are shown in **Supplementary Dataset 1**. Bar graphs show means ± s.e.m.. Asterisk indicates
429 Phosphorylation-dependent Rad53 mobility shift.

430

431 **Figure 3: High-speed, live cell imaging and super-resolution microscopy shows chromatin**
432 **expansion and enhanced flexibility following DNA damage**

433 (**a**) Diagram with representative image shows the experimental setup for high-speed imaging. Graph
434 shows MSD analysis (Δt=300 ms) of the *MET10* locus in response to Zeocin treatment indicating a
435 dose-dependent increases in global chromatin mobility in response to DNA damage ($n^{Ctr.}$=23, n^{Zeo200}=15,
436 n^{Zeo500}=21 different cells from three independent experiments). Scale bar is 2 µm. (**b**) Graphs show the
437 medians and whiskers of biophysical parameters derived from imaging data and predict chromatin
438 expansion and flexibility increases after Zeocin treatment. (**c**) Experimental outline and FACS analysis
439 of cell cycle stages. (**d**) Scheme illustrates the 3D super-resolution imaging regime. Boxplots showing
440 TetR-mCherry focus volume distributions upon Zeocin treatment in S phase cells relative to the control
441 (Ctr.) condition of multiple single cells (n numbers in graph) from two different cultures. All MSD
442 graphs represent the mean ± s.e.m. of cells pooled from three independent experiments. Boxplots in **d**
443 represent median values, interquartile ranges and whiskers. P-values, *P<0.05, **P<0.01, ***P<0.001,
444 result from unequal variances t-tests for **d** or Kolmogorow-Smirnow-Tests for **b**. Additionally, consult
445 **Supplementary Dataset 2** for mobility parameters and the number of cells analyzed.

446

447

448

449 **Figure 4: DNA damage increases chromatin flexibility**

450 **(**a) Upper panel illustrates the experimental setup and procedure for 3D intra-chromosomal distance
451 measurements between two tagged loci on Chr XIV. Boxplots and cumulative distribution graphs in
452 lower panel show GFP to mRFP distance distributions from multiple single cells (n numbers in graph)
453 from two different cultures in fixed condition before and after Zeocin treatment in G1 phase or after
454 release into S phase. (**b**) Upper panel illustrates live cell imaging regime used to monitor distance
455 changes between two loci on the left arm of Chr III over time and upon Zeocin treatment. Exemplary
456 tracks indicate the movement of CFP and mRFP foci over time. Relative MSD graph in lower panel
457 shows mean values ± s.e.m from multiple single ($n^{Ctr.}$=13, n^{Zeo}=53) cells from two different cultures and
458 indicates less constrained spot movement upon DNA damage. Boxplots represent median values,
459 interquartile ranges and whiskers and show the distribution of all measured CFP to mRFP distances. P-
460 values, *P<0.05, ***P<0.001, NS=not significant, result from unequal variances t-tests.

461

462 **Figure 5: Artificial histone reduction in the absence of damage triggers chromatin expansion and**
463 **increased motion**

464 **(**a) Schematic showing a method for H3 and H4 level reductions via transcriptional inhibition by
465 releasing cells into media containing raffinose. A plasmid borne construct in which the *GAL1/10*
466 promoter drives the only pair of histone H3/H4 genes is used in the shutdown (SD) strain whereas a
467 plasmid carrying the wild-type *HHT1-HHF1* locus is used in the control strain. (**b**) Quantified
468 Immunoblot data shows histone H4 loss at different time-points after H3/H4 shutdown in raffinose
469 medium from one experiment (**Supplementary Fig. 6**). (**c**) Boxplots and cumulative density graphs
470 show volume distributions of data derived from 3D-SIM microscopy on multiple single cells (n numbers
471 in graph) from two different cultures with tagged *MGS1* loci upon controlled histone H3/H4 shutdown.
472 Data is presented relative to the control condition (yellow with black stripes). (**d**) MSD analysis of the
473 *MGS1* locus in response to controlled histone level reductions. MSD graph in right panel shows
474 enhanced chromatin movement of the *MGS1* locus after controlled histone shutdown via 60 min release
475 into S phase in raffinose containing medium ($n^{SD(Raff)}$=30, $n^{Control(Raff)}$=34, $n^{SD(Gal)}$=52 different cells from

476 three independent experiments). MSD graph in left panel shows that G1 phase chromatin is more mobile
477 than S phase chromatin but does not further increase mobility upon H3/H4 repression in raffinose
478 containing medium ($n^{SD(Raff)}$=30, $n^{Control(Gal)}$=97 different cells from three independent experiments). All
479 MSD graphs represent the mean ± s.e.m. of cells pooled from at least three different experiments.
480 Boxplots in **d** represent median values, interquartile ranges and whiskers. P-values, ***P<0.001,
481 NS=not significant, result from unequal variances t-tests. Additionally, consult **Supplementary Dataset**
482 **2** for mobility parameters and the number of cells analyzed.

483

484 **Figure 6: Loss of high-mobility group protein Nhp6 links reduced nucleosome occupancy to**
485 **chromatin expansion and enhanced mobility**

486 (**a**) Cells carrying deletions of both NHP6A and NHP6B (*nhp6*Δ) have less nucleosomes on DNA than
487 the wild-type cells. (**b**) Immunoblot quantification from three experiments confirms reduced histone
488 levels in *nhp6*Δ cells and FACS analysis show similar cell cycle profiles for wild-type and *nhp6*Δ cells.
489 (**c-d**) MSD graphs derived from high-speed live cell imaging data of *nhp6*Δ cells (shown in dark green
490 for the *MET10* locus and in light green for the *PES4* locus) highlight enhanced chromatin mobility at
491 two independent genomic loci *MET10* and *PES4* ($n^{MET10,\ WT}$=31, $n^{MET10,\ nhp6\Delta}$=47, $n^{PES4,\ WT}$=35, $n^{PES4,}$
492 $^{nhp6\Delta}$=57 different cells from three independent experiments). (**e**) Graphs show the medians and whiskers
493 of biophysical parameters derived from imaging data and predict concurrent loss of constraining forces
494 on chromatin. Color code as in **b**. (**f**) Boxplots of *MET10* (TetR-mCherry) foci volumes resulting from
495 3D-SIM microscopy in multiple asynchronous (asy.) G1 or S phase *nhp6*Δ and wild-type cells (n
496 numbers in graph) from two different cultures indicate chromatin expansion in *nhp6*Δ cells. Color code
497 as in **b**. Bar graphs and all MSD data (cells pooled from at least three independent experiments) represent
498 the mean ± s.e.m.. Boxplots in **d** represent median values, interquartile ranges and whiskers. P-values,
499 *P<0.05, **P<0.01, ***P<0.001, result from Kolmogorow-Smirnow-Tests for **e** or unequal variances
500 t-tests for **f**. Additionally, consult **Supplementary Dataset 2** for mobility parameters and the number of
501 cells analyzed.

502

503 **Figure 7: INO80-C and checkpoint proteins regulate histone degradation and chromatin**
504 **expansion in response to damage**

505 (**a**) Representative immunoblot using H3 and H4 specific antibodies on whole cell extracts from wild-
506 type and different mutants in response to DNA damage. Rad53 was probed to confirm checkpoint
507 activation, tubulin or actin was used as loading control. (**b**) Bar graph shows immunoblot quantification
508 of wild-type, checkpoint mutants and INO80-C mutants from blots derived from n^{WT}=9, $n^{sml1\Delta}$=3,
509 $n^{mec1\Delta sml1\Delta}$=3, $n^{rad53\Delta sml1\Delta}$=3, $n^{arp8\Delta}$=3, $n^{ies4\Delta}$=3 different experiments. (**c**) Live single-cell microscopy of
510 H2B-CFP in local repair, checkpoint and INO80-C mutants upon Zeocin treatment. Graphs show the
511 mean fluorescent signals of all individual cells (cell numbers indicated in graph) per treatment over time
512 relative to the control (Ctr.) condition. (**d**) Boxplots show TetR-mCherry focus volume distributions
513 upon Zeocin treatment in wild-type and different mutant cells (n numbers in graph) from two different
514 cultures in one experiment released into S phase relative to the control (Ctr.) condition. INO80-C and
515 Mec1 are required for chromatin expansion. (**e**) Model suggesting that checkpoint signaling triggers
516 INO80-C-dependend histone loss leading to subsequent chromatin expansion, enhanced mobility and
517 chromatin flexibility which finally enhances repair. Uncropped blot images are shown in
518 **Supplementary Dataset 1**. Bar graphs **b** show means ± s.e.m.. Boxplots in **d** represent median values,
519 interquartile ranges and whiskers. P-values, *P<0.05, ***P<0.001, NS=not significant, result from
520 unequal variances t-tests. Asterisk indicates Phosphorylation-dependent Rad53 mobility shift.

521

522 **Figure 8: Reduced nucleosome occupancy enhances recombination and rescues *arp8*Δ sensitivity**

523 (**a**) Ectopic recombination assay with two different integrative *URA3* cassettes in wild-type, *arp8*Δ and
524 *nhp6*Δ strains. The diagram on the left highlights that recombination takes place in the context of
525 chromatin. Bar graphs show the mean integration frequency ± s.e.m in selected mutants relative to the
526 wild-type from three independent cultures each. (**b**) Graph showing the average recovery rate of the
527 wild-type and different isogenic mutants from an acute treatment with different Zeocin amounts relative
528 to the control condition (ctr.). Individual points indicate the mean over three independent replicas ±
529 s.e.m.. (**c**) Schematic showing the workflow and the strains for H3 and H4 level reductions by means of

530 transcriptional inhibition as in **Fig. 5a**. (**d**) Ectopic recombination assay with two different hygromycin
531 (hphMX4) based constructs which target either the *ATG2* or *MGS1* locus. Bar graphs show the mean
532 integration frequency ± s.e.m of both constructs in the SD strain relative to the Ctr. strain after 120 min.
533 pulsed histone H3/H4 reductions in Gal:Raff (galactose:raffinose, 1:20) or raffinose (Raff) medium.
534 Three independent cultures were tested. P-values, *P<0.05, ***P<0.001, result from two-tailed paired
535 students t-tests.

536

537 # Online Methods

538 **Yeast growth, cell cycle arrests and flow cytometry**

539 Yeast strains and plasmids used in this study are shown in **Supplementary Table 2 and 3**. Yeast strains
540 are all haploid and, except for the SILAC strain and the Htz1-mEos imaging control strain, derived from
541 the W303 background (**Supplementary Table 2)**. Unless otherwise stated, yeast cultures were grown
542 at 30 °C until logarithmic (LOG) growth-phase (OD_{600}=0.7; $1x10^7$ cells/ml) prior to Zeocin (Invitrogen)
543 or γIR exposure at 30°C. Live cell microscopy was done at 25 °C. Flow cytometry samples were
544 prepared as previously described[30].

545 For controlled *GAL1-10*::H3/H4 expression experiments coupled with gene targeting assays,
546 GA-8386 and the relevant control strain cultures (GA-8385) were grown overnight to saturation in YP
547 galactose/raffinose (YP Gal/Raff 1:5) medium. The next morning, cultures were inoculated in the same
548 respective medium and grown until logarithmic (LOG) growth-phase (OD_{600}=0.7; $1x10^7$ cells/ml) prior
549 to pulsed histone level reductions. After reaching LOG phase, cells were washed once and pulsed histone
550 H3 and H4 level reductions were accomplished via grown in either pre-warmed 30°C YP
551 galactose/raffinose 1:20 or YP raffinose medium for 120 minutes prior to transformation with the
552 respective gene targeting selection cassettes. For further information about the gene targeting assay,
553 please consult "Ectopic recombination assay" section.

554 For cell cycle arrest and release experiments, 1.5 x 10^{-8} M alpha factor (Zymo Research) was
555 added to exponentially growing cultures at a density of OD_{600}=0.5. After 1 hour, another half of the

556 initial alpha factor amount was added for 30 minutes and cells were either held in G1 phase or released
557 into pre-warmed medium for 15-25 minutes prior to Zeocin damage treatment in S phase. Cell fixation
558 in the relevant experiments was done for 2 minutes at room temperature with 4% Paraformaldehyde.

559 For all Zeocin or γIR exposure experiments, saturated yeast overnight cultures were diluted to
560 OD_{600}=0.1 the next morning and grown to LOG phase. In all assays, Zeocin was added directly to G1
561 arrested, S phase released or asynchronously growing LOG cultures. Cultures were incubated with the
562 drug for 1 h prior to high-speed tracking microscopy or the indicated amount time periods for other
563 assays and experiments (**Main Figures and Supplementary Figures**). For γIR exposure, 5ml of cell
564 culture was transferred to a 35x10mm petri dish and irradiated in a Faxitron CellRad cell-irradiator until
565 the indicated dose (Grey) was reached. After γIR treatment, cells were directly harvested for further
566 downstream Western blot or mass-spectrometry-based analysis. For undamaged conditions, cells were
567 either imaged immediately for high-speed tracking microscopy or growth was continued along with the
568 treated samples for the indicated time periods. γIR undamaged control cells were also spread on petri
569 dishes and harvested after irradiation of treated cells was completed. Further specific growth and
570 treatment conditions for high-speed tracking live cell microscopy were done according to Seeber *et al.*[12].

571 The proteasome inhibition assay with proteasome inhibitor MG132 (Bachem) was done
572 according to Liu *et al.*[31]. In brief, wild-type GA-6879 (**Fig. 2a**) or *erg6*Δ[32] GA-1364 (**Fig. 2b**) cells were
573 grown to saturation overnight in SC proline (wild-type, SC medium without ammonium sulfate but 0.1%
574 L-proline) or YPAD medium (GA-1364). The next morning, cells were inoculated to OD_{600}=0.1 in SC
575 (wild-type) or YPAD (GA-1364) proline medium supplemented with 0.003% sodium dodecyl sulfate
576 (SDS) and grown to OD_{600}=0.5 before addition of 75 μM MG132 or the same volume of DMSO for the
577 control condition. After 30 min. incubation with the inhibitor, Zeocin treatment or no-damage control
578 growth was performed for 1 hour at 30°C prior to cell harvesting for Western blot analysis.

579 For H2B-CFP (Strain GA-3364 and derivatives) and 2-foci (Strain GA-9777) live cell
580 fluorescent microscopy, LOG phase cells were trapped with 3 pulses of 5 psi pressure in CellASIC plates
581 of the ONIX microfluidic perfusion system (Merck Millipore). All perfusions were done at a continuous
582 flow rate of 2 psi pressure. After a 20-30 minute recovery phase, cells were treated for 30 minutes with
583 the indicated amount of Zeocin prior to high-speed CFP-RFP tracking microscopy. The recovery phase

584 of H2B-CFP tagged cells was 20 minutes after which they were treated with a pulse of Zeocin for 1 hour
585 and H2B-CFP fluorescence was followed for additional 40 minutes after treatment.

586 For constitutive H3/H4 expression or reduction experiments, GA-8386 and the relevant control
587 strain cultures (GA-8385) were grown overnight to saturation in YP Galactose (YP Gal) or YP
588 galactose/raffinose (YP Gal/Raff) medium and inoculated in the same respective media prior to Zeocin
589 treatment and cell harvest. For controlled H3/H4 shutdown experiments, overnight growth and growth
590 to OD600=0.5 was done with the same strains in YP Gal/Raff (Gal/Raff 1:5 ratio) medium which confers
591 wild-type H3/H4 expression levels. After G1 phase arrest at 25°C with alpha factor in YP Gal/Raff
592 medium, cells were released either into pre-warmed 25°C YP Gal or YP Raff medium for 60 minutes
593 prior to fixation for structural illumination microscopy (SIM) or live cell high-speed imaging.

594 In all other Western blot and label-free mass spectrometry experiments, cells were grown in full
595 medium (YPD) and cell growth for microscopy experiments was either done in synthetic complete (SC)
596 medium or sterile filtered, non-autoclaved YPD medium.

597 **Genome-wide nucleosome mapping**

598 Strains tested for changes in nucleosome occupancy (GA-6879 and GA-8386) were grown in
599 appropriate media to OD_{600}=0.8. Cultures were split into two and one of them was treated with Zeocin
600 (500µg/ml) for 1 hour. At this point the OD_{600} absorbance of each sample was measured and *Candida*
601 *glabrata* cells were spiked in to 1/10 according to the sample OD_{600}. Cells were washed three times with
602 ice cold TBS (20mM Tris-HCl pH 8.0 and 150mM NaCl) and lysed by beat beating in micrococcal
603 nuclease (MNase) digestion buffer (10 mM Tris pH 8.0, 50 mM NaCl, 5mM MgCl2, 1 mM CaCl2,
604 1mM beta-mercaptoethanol, 0.5 mM spermidine, 0.075% NP40). The obtained chromatin samples were
605 MNase digested to isolate mono-nucleosomes and sequencing libraries were prepared according to the
606 method described in Wiechens *et al.*[33]. Paired end libraries of MNase digested chromatin were
607 sequenced using illumina HiSeq technology. Fastq files containing raw reads were aligned to the *S.*
608 *cerevisiae* and *C. glabrata* reference genomes by Bowtie2 with option of maximum fragment length
609 500 for nucleosome fragments. The nucleosome dyads at each position were calculated in a defined
610 window flanking the transcription start site (TSS). The sum of dyads at a given position across all TSS

611 was then normalized by the total number of nucleosome dyads across all position flanking ~ 6000 TSSs
612 in the given window. The reads were further normalized by dividing the fraction of *C. glabrata* reads in
613 the sample. For low and high expression gene plots, the TSS of 15% highly and 15% lowly expressed
614 genes were chosen. The data was smoothed using a 50 bp sliding window for graphical representation.
615 Plots were generated with python's plotting modules matplotlib and pylab.

616 **Quantitative Western Blot Analysis**

617 The total protein content in the relevant samples was determined with the Quant-iT protein assay kit
618 (ThermoFisher Scientific) and 8.75 µg of total protein was loaded and run on Criterion TGX Stain-Free
619 8-16% (Biorad) gels under SDS denaturing electrophoresis conditions. Rapid fluorescent detection of
620 all proteins in the gel or on the membrane was done according to the manufacturer's specifications and
621 protein transfer on PVDF membranes was performed using the Trans-Blot Turbo system. All antibodies
622 used for subsequent immunodetections are listed in **Supplementary Table 4**. Rad53 protein was
623 detected using a custom-made mouse monoclonal antibody (GenScript) against FHA2 domain of Rad53.
624 Anti-γH2A was similarly a custom-made polyclonal antibody, that is specific for phospho-S129 in yeast
625 H2A. Titration curves of histone H3 and histone H4 antibodies done to work within the linear detection
626 range prior to use (**data not shown**).

627 **Chromatin Fractionation and Quantitative Mass Spectrometry**

628 For SILAC based mass spectrometry, lysine and arginine double labeling of the *lys2Δ arg4Δ* strain yAG-
629 06A was achieved by growth for at least ten generations in "heavy" medium as described previously in
630 Gruhler *et al.*[34]. After growth to LOG phase or at G1 cell cycle arrest, "light" labeled cells (or "heavy"
631 labeled cells for label-swap controls) were treated for 1h with Zeocin and mixed 1:1 based on exact cell
632 count with "heavy" labeled ("light" for label-swap control), non-treated control cells. Prior to mixing,
633 FACS and Western blot samples were taken to test for cell cycle distribution and DDC activation.

634 Chromatin fractionation was performed as previously described[35] with the modification that
635 chromatin obtained from SILAC labeled yeast samples was resuspended in urea buffer (50 mM Tris-
636 HCl pH 7.5, 6 M Urea, 1% SDS, 5 mM EDTA) sonicated for optimal solubilizing of proteins followed
637 by a TCA protein precipitation step prior to downstream mass spectrometric analysis. To avoid

638 carbamylation in urea buffer, samples were kept below 20°C and quickly processed. Control samples
639 from whole cell extract (WCE), supernatant (SUP) and chromatin fraction (CHR) were analyzed with
640 SDS-PAGE (Novex 8–16% Tris-Glycine Gel, Invitrogen) gel electrophoresis followed by Coomassie
641 staining.

642 Samples for label-free histone quantification came from LOG phase or G1 phase arrested cells
643 grown in YPD medium. After γIR treatment, 5 ml of culture were fixed with 10% TCA on ice. Whole
644 cell lysates were obtained with bead-beating cells at 4°C in urea buffer (50 mM TRIS pH 7.5, 6 M Urea,
645 1% SDS, 5 mM EDTA). 100-150 µg total protein was precipitated for downstream MS analysis.

646 For both SILAC and label-free samples, reduction and alkylation of cysteines was performed in
647 20 µl RCM buffer by adding 4 µl 100 mM TCEP for 30 min followed by 4 µl 250mM iodoaeetamide
648 for another 30 min (in the dark), both at room temperature. Prior to the addition of 20 µl of 1 mg/ ml
649 LysC (Wako, Japan) the extracts were twofold diluted to keep a final HEPES concentration of 20 mM.
650 The first digest was performed overnight at 25°C. After 2-fold dilution, 100 µl of 0.5 mg/ ml trypsin
651 was added and the second digest was performed at 37°C overnight. Samples were desalted using SepPak
652 C18 columns (Waters) and eluates were dried to completion in a SpeedVac (ThermoFisher Scientific).

653 Both SILAC and label-free LC/MS/MS analyses was performed on an Easy-nLC 1000 pump
654 coupled to an LTQ Orbitrap Velos mass spectrometer (ThermoFisher Scientific) using a Digital
655 PicoView ion source (New Objective). Peptides were separated on a New Objective analytical column
656 (75 µm x 25 cm, Reprosil, 3 µm) with a 150 min. 0.1% formic acid/acetonitrile gradient. The flow rate
657 was 200 nL/min and injection volumes were adapted accordingly for 1 µg peptides on column.
658 Data were acquired in a Top20 data dependent analysis mode. MS scans were acquired at a resolution
659 of 60000 over a range of *m/z* 350 to 1200. Label-free peptides were identified searching SwissProt using
660 Mascot 2.4 (Matrix Science) and compiled in Scaffold 3.0 (Proteome Software). SILAC peptides were
661 identified with MaxQuant 1.4.1.2. searching the SGD database. Two missed cleavage sites were
662 allowed.

663 Label-free relative quantification of histones was done by generating the extracted ion
664 chromatogram for the peptide precursor mass, integrating the peak areas (using QuanBrowser,

665 ThermoFisher Scientific) which are then used for calculating the peptide ratios. The average of those
666 ratios determines the ratio of the histones (reference untreated or wild type sample). This method is more
667 precise than the TOP 3 TIC method used in Scaffold. Untreated or wild type references were set to 1.
668 We used 2 peptides from each ALF, KPK1, IF4A and IFSA1 protein as internal references for the
669 quantification of relative histone abundances in each run. Histone level ratios in SILAC samples are
670 shown as the average from all non-label-swap or label-swap replicas. Ratios were derived from the
671 MaxQuant peptide list taking into account only core histone peptides reported as not being subject to
672 post translational modifications[21]. Significance was addressed by blotting the distribution of all protein
673 ratios from the MaxQuant protein-groups list together with the protein intensities. Core histones were
674 always the most abundant proteins measured and reside within the first significant interval. The
675 MaxQuant protein-groups list was filtered by removing all contaminants, all reverse hits and proteins
676 quantified with less than 2 peptides. The cutoff for variability was set to 30%. Normalization was done
677 manually taking the 35 most abundant proteins (histones excluded). The MaxQuant peptide list (except
678 for the G1 experiment) was filtered accordingly without variability cutoff and only taking peptides into
679 account that had a L/H or H/L count greater than 3. Normalization was done manually taking the top
680 10% most abundant peptides (histone peptides excluded).

681 **Live cell microscopy and Image Analysis**

682 Live microscopy was done on a temperature controllable Olympus IX81 microscope with a Yokogawa
683 CSU-X1 scanning head equipped with two EM-CCD EvolveDelta (Photometrics) cameras, an ASI MS-
684 2000 Z-piezo stage and a PlanApo x100, NA 1.45 total internal reflection fluorescence microscope oil
685 objective and Visiview software. For mRFP-GFP or mRFP-CFP high-speed tracking, fluorophores were
686 excited with lasers at 561 nm (mCherry or mRFP) and 491 nm (GFP) or 440 nm (CFP) and emitted
687 fluorescence was acquired simultaneously on separate cameras (Semrock FF01-617/73-25 filter for
688 mCherry/mRFP and Semrock FF02-525/40-25 filter for GFP or Semrock FF01-475/42-25 for CFP).
689 High-speed time-lapse series were conducted taking 8 optical slices per stack either every 80 ms for 1
690 min or 300 ms for 2 min, with 10 ms exposure times per slice respectively. Time-lapse image stacks
691 were analyzed as in Dion *et al.*[9], using a custom made ImageJ (FIJI) plug-in[36] to extract coordinates of
692 locus position from the movies. Phototoxicity was tested by exposing wild-type cells (GA-6879) to

693 standard imaging conditions and following outgrowth for 5 h by morphological analysis, comparing
694 them with unexposed cells. Time-series acquired from Strains GA-9227 and GA-9777 (Two-spot data)
695 were deconvolved using Huygens Remote Manager, channel-aligned and cropped to contain one single
696 cell/nucleus with the two respective fluorescent spots. Spot tracking over time was done with the ImageJ
697 plugin TrackMate included in Fiji[37]. Boxplot graphs were generated by plotting all measured distances
698 of treated or untreated cells. Relative MSD analysis was performed with KNIME[38] using the workflow
699 provided in the supplementary information (**Supplementary Dataset 2**). For each frame, the distance
700 vector of tracks in two channels was measured by selecting the two spots with minimal distance. We
701 performed an MSD analysis on the distance vectors for all frames and tracks with a maximum MSD(t)
702 value bigger than 10 µm² were considered as outliers (due to mis-matching two distant tracks) and
703 removed from the analysis. Relative MSD vs. t was averaged over all tracks and plotted using R.

704 For H2B-CFP (GA-3364 and derivatives) live cell microscopy, cells trapped in CellASIC plates
705 were mounted on the same microscopic setup and different stage positions of the whole field of view
706 were excited with a 440nm laser and the emitted fluorescence was acquired on a EM-CCD EvolveDelta
707 (Photometrics) camera using a Semrock FF01-475/42-25 emission filter. The Htz1-mEos (GA-9594)
708 and Nup49-GFP (GA-5816) control strain was excited at 491 nm and fluorescence was recorded through
709 a Semrock FF02-525/40-25 filter. Time-lapse series (120 min total) of 100 optical slices per stack
710 (200nm intervals) were acquired for 12 time points at 10 min intervals, with each slice being exposed
711 for 10 msec per laser line. Bright-field images were acquired using a CoolLED diode. Images were
712 deconvolved using the Huygens Remote Manager software. For image analysis, deconvolved maximum
713 intensity projections were analyzed as a merged stack in ICY. Nuclei were detected and segmented using
714 HK means and active contours and followed through the time series. The integrated nuclear intensity
715 was calculated for each cell nucleus and the average intensity of all single cells per condition was plotted
716 over time. The t0 time-point to 100% intensity (via average of the first two timepoints) and the Zeocin
717 treatment condition of each strain is shown relative to its control.

718 **Structured Illumination Microscopy and Image Analysis**

719 Structured illumination images were acquired on a Zeiss Elyra S.1 microscope with a Andor iXon 885
720 EMCCD camera using a HR diode 488 100nW solid state laser, BP 525-580 + LP 750 filter and a PLAN-

721 APOCHROMAT 63x N.A. 1.4 oil DIC objective lens. Cells were first fixed in PFA 4%, washed 3 times
722 in PBS and then attached to a thin SIM grade Zeiss 1.5 glass coverslip using Concanavalin A. Cells
723 were fully sectioned by 50-65 slices with 0.1 nm intervals taken at 60 ms exposures per slice using 5
724 rotations of the illumination grid. Brightfield images of the cells were also acquired using an X-Cite PC
725 120 EXFO Metal Halide lamp. Zen Black was used to process the images using automatic settings with
726 the Raw Scale option selected. 3D stacks were then analyzed by using pixel classification and a custom
727 Matlab script to determine the spot volumes and other features as follows. We used a fully automated
728 nucleus and spot segmentation workflow that allowed the individual detection and feature extraction
729 where a manual or even a semi-automated delineation would be unfeasible. The image processing
730 software was realized within the MATLAB environment and supported by the supervised learning-
731 based pixel classification toolkit Ilastik[39]. The voxels corresponding to the nucleus, the inner spot and
732 background regions are annotated interactively by brush strokes during the training phase. Features
733 calculated at the labeled pixels and their local neighborhood are then used to train a pixel classifier based
734 on a Random Forest ensemble learning method. The processing software provides an automated whole
735 segmentation of all the nuclei and spots present in the scene. The image processing function is later used
736 in a parallelized batch process on multiple processors. After detection and segmentation of nuclei and
737 spots, the program produces a graphical output in form a maximum intensity projection with delineation
738 of the nucleus, the spots and the unique ID integer that identifies the nucleus candidate. In addition, 3D
739 logical masks corresponding to the classes “spot” and “nucleus” are computed. Finally, the program
740 generates an ascii file where the key features like volume and solidity 3D and descriptive statistics are
741 listed for all detected nuclei and foci. The solidity factor is calculated as the proportion of pixels in the
742 3D convex hull. For statistical analysis and data representation, raw volumes were filtered to exclude
743 spots smaller than 200 and greater than 4000 voxels, the control (Ctr.) condition was set to 1 and Zeocin
744 treated spot or nuclei volume distributions are shown relative to the untreated control. The distributions
745 were plotted with R as boxplot graphs or a cumulative density functions.

746 **Microscopy and Image Analysis of Fixed Samples**

747 Microscopy of fixed GA-9777 samples was done with the same Olympus IX81 microscope setup
748 mentioned before. Cells were fixed with paraformaldehyde and attached to a thin SIM grade Zeiss 1.5

749 glass coverslip using Concanavalin. We acquired 70 optical slices in 100nm intervals with the 561 nm
750 and 491 laser line (130 ms exposure each). Bright-field images were acquired using a CoolLED diode.
751 Images were deconvolved using Huygens Remote Manager, channel-aligned and 3D inter-spot distances
752 (Δd) between the GFP and mRFP centroids were measured with the Imaris software. The distribution of
753 all measured distances per condition was plotted with R as a boxplot graph or a cumulative density
754 function.

755 **Ectopic Recombination Assays**

756 For **Fig. 8a**: As used in wild-type cells, *arp8*Δ cells and cells depleted for *NHP6A*/*NHP6B*

757 For specific growth conditions, please consult the "*Yeast growth, cell cycle arrests and flow cytometry*"
758 section. Equal amounts of exponentially growing wild-type (GA-6879) *arp8*Δ (GA-8132) and *nhp6*Δ
759 (GA-9771) were transformed with the transformation protocol either with a linearized *URA3* plasmid
760 (pRS406 cut with *Stu*I) presenting 800 bp homology to the W303 *ura3-1* locus or a *mgs1::caURA3* PCR
761 fragment (template plasmid #1050) presenting 40 bp and 42 bp upstream and downstream homology to
762 the *MGS1* locus. As a control, the centromeric circular plasmid #2422 (ADE2, hphMX4, Cen/ARS),
763 which is maintained in yeast cells ectopically, was transformed alongside with the URA3 integration
764 cassettes. Primers were #7297:

765 (GTTTTTTTACGCTTGAGGCGCATTGCATTGCTGGCACGTTTTTGTGCGGATCC
766 CCGGGTTAATTAA) and #7298:

767 (CGTATATGTTCTAATATATCTCAGATGGGCCCGCGAGACTTTGCGCGTTGGCCGATTCAT
768 TA).

769 After transformation, cells were split and plated on SC-URA plates (100 µl) to select for transformants
770 resulting from integration and on and YPD + Hygromycin B plates to select for cells containing the
771 plasmid. The numbers of Ura+ and Leu+ transformants obtained from each reaction were compared to
772 calculate the relative integration rate for each strain, with that of a wild-type strain arbitrarily set to 1 as
773 a reference. Growth was scored in biological quadruplicates and each transformation was done with four
774 technical replicates.; results were averaged.

775 For **Fig. 8c-d**: "Ctr." cells and Gal:H3/H4 "histone shutdown" cells

776 For specific growth conditions, please consult the "*Yeast growth, cell cycle arrests and flow cytometry*"
777 section. After pre-growth in YP Galactose/Raffinose 1:5 medium, equal amounts of exponentially
778 growing control (GA-8385) and Gal:H3/H4 "histone shutdown" (GA-8386) cells were pulse-reduced
779 for histone H3 and H4 levels via 2 hour growth in either YP Galactose/Raffinose 1:20 or YP Raffinose
780 medium. After the histone-reduction pulse, transformations were done with either an *atg2::hphMX4*
781 PCR fragment (PCR product – *ATG2::hygro*, template plasmid #1049) presenting 40 bp and 40 bp
782 upstream and downstream homology to the *ATG2* locus or a *mgs1::hphMX4* PCR fragment (PCR
783 product – *MGS1::hygro*, template plasmid #1049) presenting 40 bp and 42 bp upstream and downstream
784 homology to the *MGS1* locus. As a control, the centromeric circular plasmid #282 (LEU2, Cen/ARS),
785 which is maintained in yeast cells ectopically, was transformed alongside with the hphMX4 PCR
786 integration cassettes.

787 Primers for PCR product – *ATG2::hygro* were #6302:

788 (ATAGCCTTGGCGAGTTTTCCGTACATTGAAGAATTCGCCAAGCGGATGCCGGGAGCAGA
789 C)

790 and #6303:

791 (GGGATTTTTGGCTCAAGGTGTGGTGGCCCCTTTTCTAAGGGTGAGCTGATACCGCTCGCC)

792 Primers for PCR product – *MGS1::hygro* were #7297:

793 (GTTTTTTTACGCTTGAGGCGCATTGCATTGCTGGCACGTTTTTGTGCGGATCCCCGGGTTA
794 ATTAA)

795 and #7298:

796 (CGTATATGTTCTAATATATCTCAGATGGGCCCGCGAGACTTTGCGCGTTGGCCGATTCAT
797 TA).

798 After transformation, cells were split and plated on YPGal +Hygromycin B plates (100 µl plated) to
799 select for transformants resulting from integration of *ATG2::hygro* or *MGS1::hygro* and on and SCGal
800 -LEU plates (10 µl plated) to select for cells containing the plasmid. The numbers of hphMX4+ and
801 LEU+ transformants obtained from each reaction were compared to calculate the relative integration

802 rate for each strain, with that of a wild-type strain arbitrarily set to 1 as a reference. Growth was done in
803 biological quadruplicates and each transformation was done with four technical replicates; results were
804 averaged.

805 **Recovery assay**

806 Equal amounts of exponentially growing (YPAD medium, cell density approx. $1x10^7$ cells/ml) WT (GA-
807 6879), *arp8*Δ (GA-8132), *nhp6*Δ (GA-9771) and *arp8*Δ*nhp6*Δ cells (GA-9815) were treated in
808 triplicates with increasing amounts of Zeocin (100, 250 and 500 µg/ml). After 1 hour of treatment, cells
809 were washed once with fresh, pre-warmed (30°C) YPAD medium and grown for an additional hour in
810 YPAD without Zeocin. After this step, the cell density was accurately determined in three technical
811 replicates and used as a later correction factor for cell growth within the 1 hour of Zeocin treatment and
812 the 1 hour growth in YPAD of the control (Ctr.) versus the Zeocin treated cultures (Zeo^{100} – Zeo^{500}).
813 Aliquots were removed and plated in a dilution row. Growing colonies vs. plated cells were quantified,
814 the Ctr. situation served as reference point and was set to 100%.

815 **Rad52-YFP Recovery Assay**

816 Cells grown to saturation overnight in sterile filtered, non-autoclaved YPD medium were diluted the
817 next morning and the experiment was started when reaching OD_{600}=0.6. Wild type (GA-9772) and
818 *nhp6*Δ cells (GA-9771) were treated with 250 µg/ml Zeocin for 30 minutes. Zeocin was washed away
819 and Rad52-YFP foci formation was followed over a total time-course of 16 hours taking microscopic
820 images at the following time points: 0 min, 20 min, 40 min, 1h, 2h, 4h, 6h, 8h, 10h, 12h, 14h and 16h.
821 Rad52-YFP foci were imaged with the same microscopic setup as mentioned above acquiring 50 optical
822 slices in 200 nm intervals with 50 ms exposure time using a 514 nm laser with appropriate emission
823 filters. Images were deconvolved as described above, maximum intensity projected and the binary (+ or
824 -) content of Rad52-YFP foci all living cells at each time point in each strain was counted. The average
825 amount of Rad52-YFP foci containing cells per time point was plotted and is shown together with a
826 logarithmic fit.

827 **Estimating the anomalous diffusion exponent α and the diffusion coefficient**

828 Please refer to Supplementary Notes.

829 **Estimating the effective spring coefficient k_c**

830 Please refer to Supplementary Notes.

831 **Statistics and Reproducibility**

832 All chromatin mobility data (spot tracking) are pooled from three independent experiments (**Fig. 3a,**
833 **Fig. 5d, Fig. 6cd, Supplementary Fig. 5a**). Statistical analysis testing the significance of the
834 biophysical parameters derived from the imaging data was performed with Matlab using the
835 Kolmogorow-Smirnow-Test (**Fig. 3b, Fig. 5d, Fig. 6e, Supplementary Fig. 5b, Supplementary Fig.**
836 **7cd**). All SIM microscopy data from individual single cells are pooled and were derived from one
837 experiment. The data was analysed with RStudio using unequal variance t-tests (**Fig. 3d, Fig. 5c, Fig.**
838 **6f, Fig. 7d**). For H2B-CFP single cell fluorescent microscopy analysis, the integrated nuclear intensity
839 was calculated for each cell nucleus and the average intensity of all single cells per condition was plotted
840 over time. All data from single cells originating from three independent cultures on three different days
841 (**Fig. 1d H2B-CFP**); two independent cultures on two different days (**Fig. 1d** Htz1-mEos, **Fig. 7c**
842 *rad51*Δ*/sml1*Δ*/arp8*Δ); two independent cultures from the same day (**Fig. 7c** *rad53*Δ*sml1*Δ).
843 Recombination efficiency and cell recovery experiments were performed in triplicates (three
844 independent cell cultures) and Excel was used to perform two-tailed student's t-tests (**Fig. 8 abd**).
845 Chromatin fractionations were repeated with three independent cultures (**Supplementary Fig. 1fg**) or
846 two independent cultures (**Fig. 1a, Supplementary Fig. 1h, Supplementary Fig. 3ij**). Nucleosome
847 mapping data for the wild-type strain (GA-6879) was performed on four independent cultures (**Fig. 1c,**
848 **Supplementary Fig. 2e**); for the H3/H4 transcription independent strain (GA-8386) the experiment was
849 done once (**Supplementary Fig. 4b**) but new data deriving from four independent cultures shows the
850 same effect (**data not shown**). The kinetics of the Rad52-YFP recovery assay on wild-type and *nhp6*Δ
851 cells (12 different time-points) was performed once but done on the single cell level.

852 **Data availability statement**

853 The EBI project ID for the nucleosome-Seq data in this study is PRJEB14701. Source data for Figs.
854 1bd, 2abc, 5b, 7bc, 8a, Supplementary Fig. 2g and mass spectrometry data (Supplementary Dataset 4-
855 9) are available with the paper online. Other data supporting the findings of this study are available from

856 the corresponding authors upon request.

857

858 ## References (Online Methods only)

859 30. Haase, S.B. & Lew, D.J. Flow cytometric analysis of DNA content in budding yeast. *Methods*
860 *Enzymol* **283**, 322-32 (1997).

861 31. Liu, C., Apodaca, J., Davis, L.E. & Rao, H. Proteasome inhibition in wild-type yeast
862 Saccharomyces cerevisiae cells. *Biotechniques* **42**, 158, 160, 162 (2007).

863 32. Lee, D.H. & Goldberg, A.L. Selective inhibitors of the proteasome-dependent and vacuolar
864 pathways of protein degradation in Saccharomyces cerevisiae. *J Biol Chem* **271**, 27280-4
865 (1996).

866 33. Wiechens, N. et al. The Chromatin Remodelling Enzymes SNF2H and SNF2L Position
867 Nucleosomes adjacent to CTCF and Other Transcription Factors. *PLoS Genet* **12**, e1005940
868 (2016).

869 34. Gruhler, A. et al. Quantitative phosphoproteomics applied to the yeast pheromone signaling
870 pathway. *Mol Cell Proteomics* **4**, 310-27 (2005).

871 35. Pasero, P., Duncker, B.P., Schwob, E. & Gasser, S.M. A role for the Cdc7 kinase regulatory
872 subunit Dbf4p in the formation of initiation-competent origins of replication. *Genes &*
873 *Development* **13**, 2159-2176 (1999).

874 36. Sage, D., Neumann, F.R., Hediger, F., Gasser, S.M. & Unser, M. Automatic tracking of
875 individual fluorescence particles: application to the study of chromosome dynamics. *IEEE*
876 *Trans Image Process* **14**, 1372-83 (2005).

877 37. Schindelin, J. et al. Fiji: an open-source platform for biological-image analysis. *Nat Methods* **9**,
878 676-82 (2012).

879 38. Dietz, C. & Berthold, M.R. KNIME for Open-Source Bioimage Analysis: A Tutorial. *Adv Anat*
880 *Embryol Cell Biol* **219**, 179-97 (2016).

881 39. Sommer, C. & Gerlich, D.W. Machine learning in cell biology - teaching computers to
882 recognize phenotypes. *J Cell Sci* **126**, 5529-39 (2013).

883

884

Figure 1

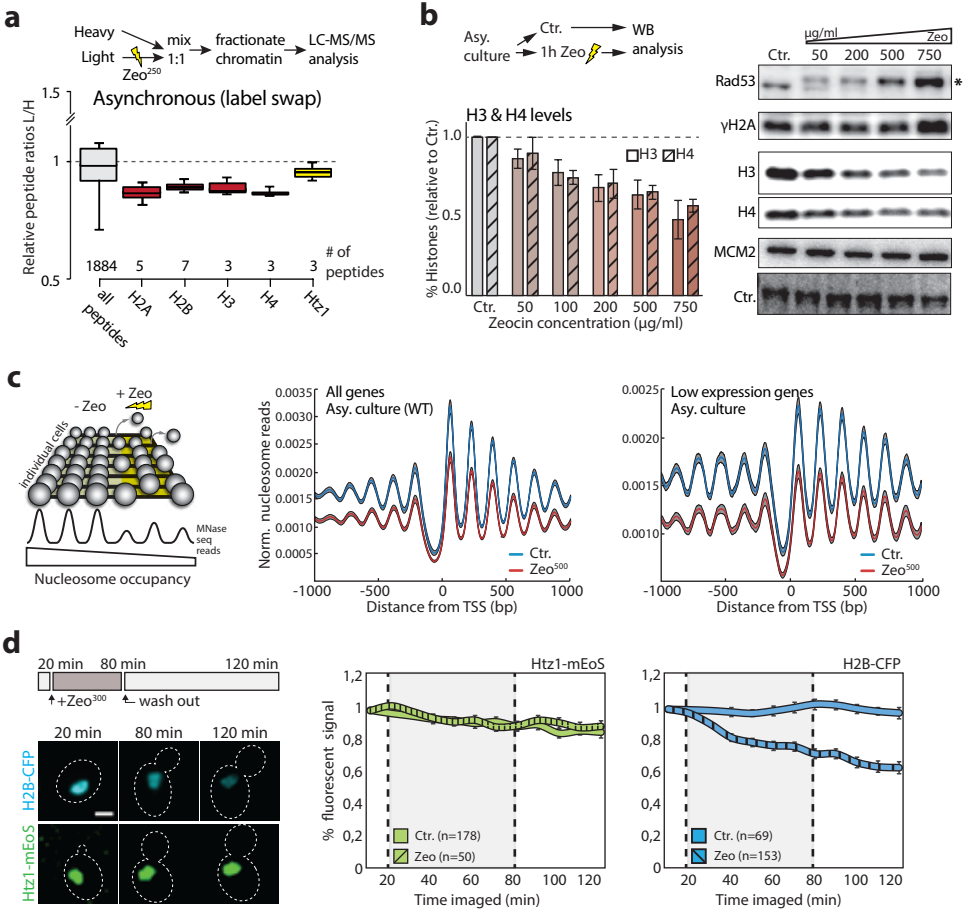
a
Heavy
Light
Zeo250
mix
1:1
fractionate chromatin
LC-MS/MS analysis
Asynchronous (label swap)
Relative peptide ratios L/H
1.5
1
0.5
1884
5
7
3
3
3
# of peptides
all peptides
H2A
H2B
H3
H4
Htz1
b
Asy. culture
Ctr.
1h Zeo
WB analysis
H3 & H4 levels
% Histones (relative to Ctr.)
1.0
0.5
0.0
H3
H4
Ctr.
50
100
200
500
750
Zeocin concentration (µg/ml)
µg/ml
Zeo
Ctr.
50
200
500
750
Rad53
γH2A
H3
H4
MCM2
Ctr.
c
- Zeo
+ Zeo
individual cells
MNase seq reads
Nucleosome occupancy
All genes
Asy. culture (WT)
Norm. nucleosome reads
0.0035
0.0030
0.0025
0.0020
0.0015
0.0010
0.0005
Ctr.
Zeo500
-1000
-500
0
500
1000
Distance from TSS (bp)
Low expression genes
Asy. culture
0.0025
0.0020
0.0015
0.0010
Ctr.
Zeo500
-1000
-500
0
500
1000
Distance from TSS (bp)
d
20 min
80 min
120 min
+Zeo300
wash out
20 min
80 min
120 min
H2B-CFP
Htz1-mEoS
Htz1-mEoS
% fluorescent signal
1,2
1
0,8
0,6
0,4
0,2
0
Ctr. (n=178)
Zeo (n=50)
20
40
60
80
100
120
Time imaged (min)
H2B-CFP
1,2
1
0,8
0,6
0,4
0,2
0
Ctr. (n=69)
Zeo (n=153)
20
40
60
80
100
120
Time imaged (min)

Figure 2

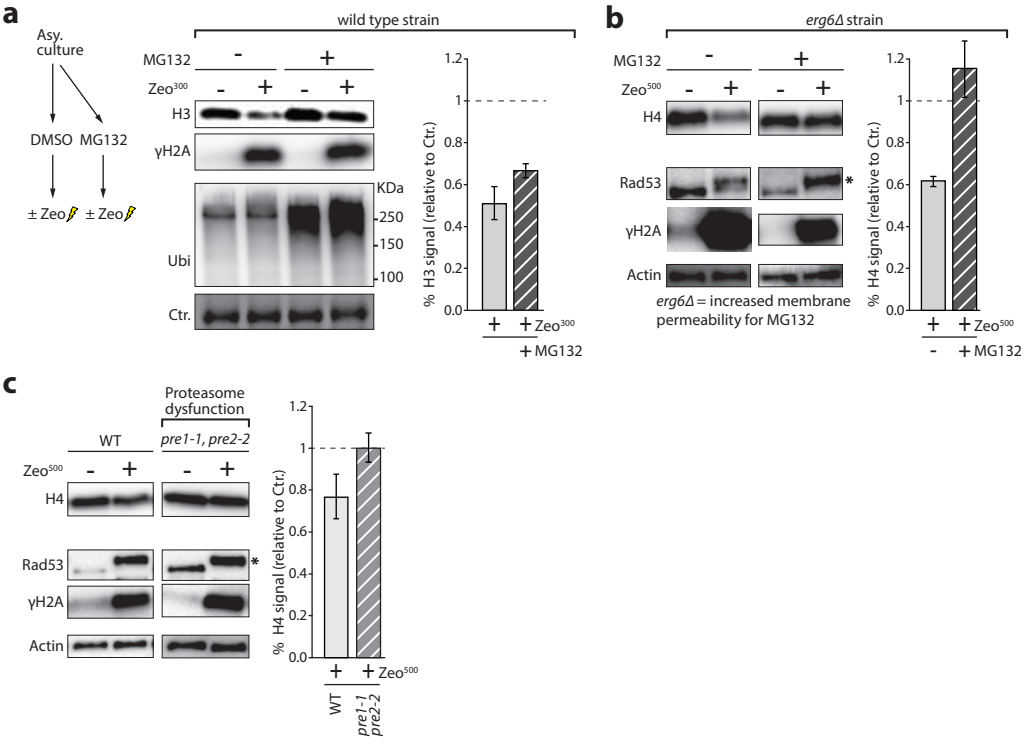
a
Asy. culture
DMSO
MG132
± Zeo
± Zeo
wild type strain
MG132
Zeo300
H3
γH2A
Ubi
Ctr.
KDa
250
150
100
% H3 signal (relative to Ctr.)
+ Zeo300
+ MG132
b
erg6Δ strain
MG132
Zeo500
H4
Rad53
γH2A
Actin
erg6Δ = increased membrane permeability for MG132
% H4 signal (relative to Ctr.)
+ Zeo500
+ MG132
c
Proteasome dysfunction
WT
pre1-1, pre2-2
Zeo500
H4
Rad53
γH2A
Actin
% H4 signal (relative to Ctr.)
+ Zeo500
WT
pre1-1 pre2-2

Figure 3

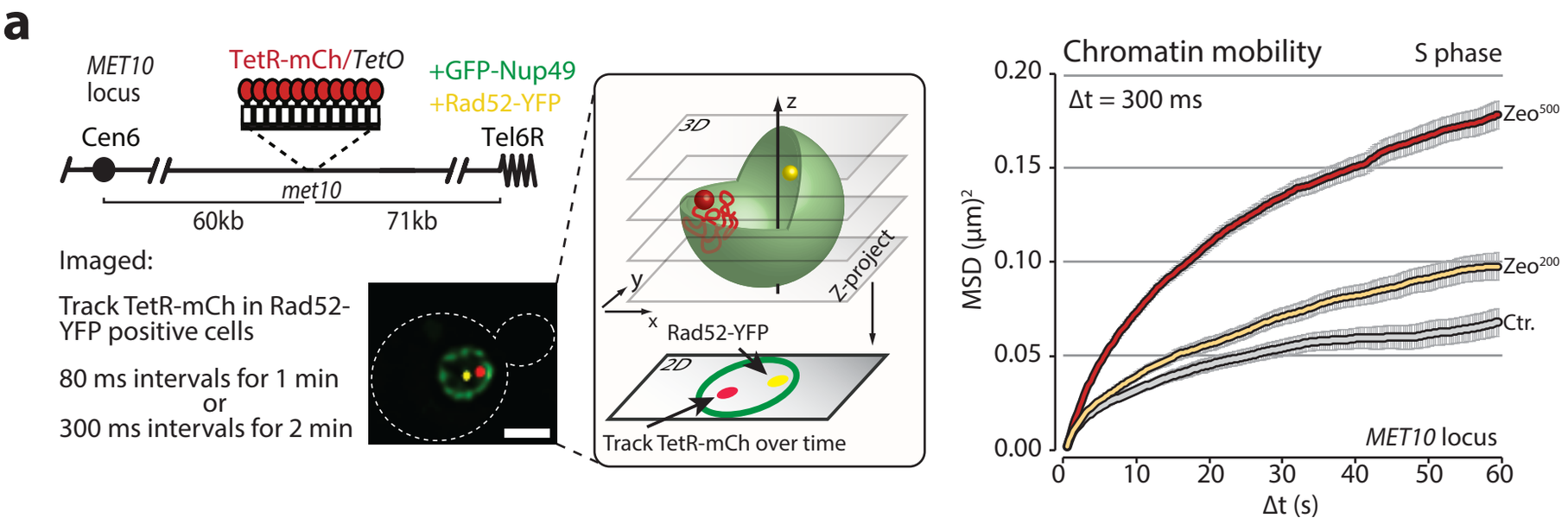
a
MET10 locus
TetR-mCh/TetO
+GFP-Nup49
+Rad52-YFP
Cen6
Tel6R
met10
60kb
71kb
Imaged:
Track TetR-mCh in Rad52-YFP positive cells
80 ms intervals for 1 min
or
300 ms intervals for 2 min
3D
z
y
x
Z-project
Rad52-YFP
2D
Track TetR-mCh over time
Chromatin mobility
S phase
Δt = 300 ms
MSD (μm)²
Zeo500
Zeo200
Ctr.
MET10 locus
Δt (s)

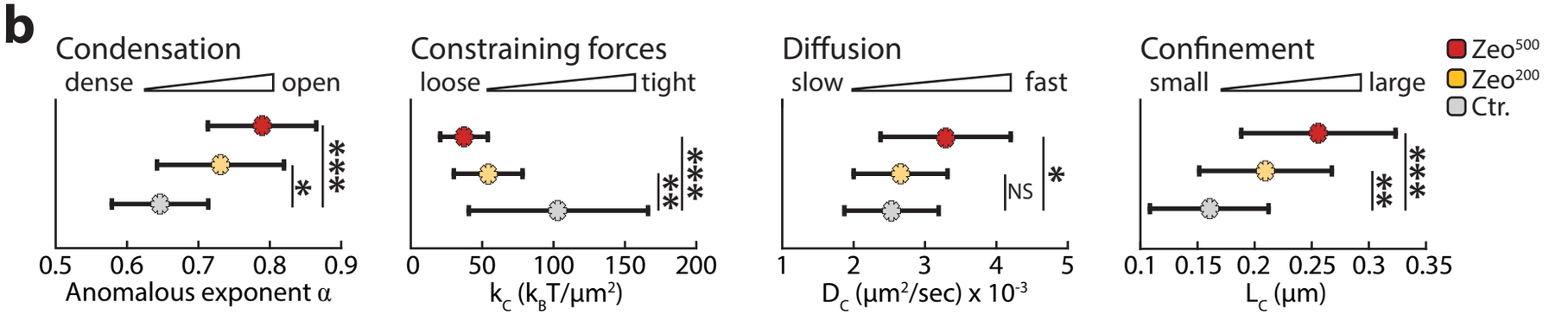
b
Condensation
dense
open
Anomalous exponent α
Constraining forces
loose
tight
kC (kBT/μm²)
Diffusion
slow
fast
NS
DC (μm²/sec) x 10⁻³
Confinement
small
large
LC (μm)
Zeo500
Zeo200
Ctr.

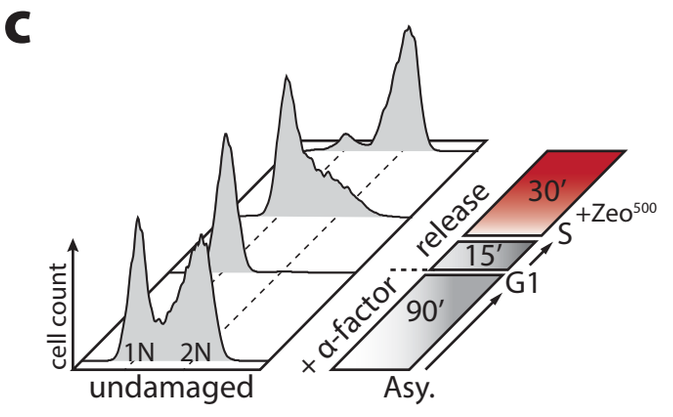
c
cell count
1N
2N
undamaged
+ α-factor
release
30′
+Zeo500
15′
S
G1
90′
Asy.

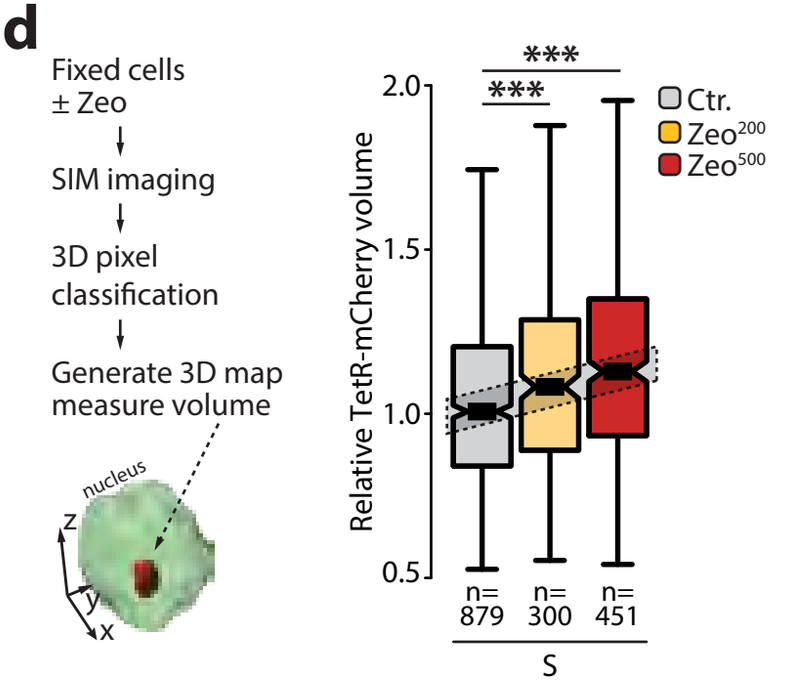
d
Fixed cells
± Zeo
SIM imaging
3D pixel classification
Generate 3D map measure volume
nucleus
z
y
x
Relative TetR-mCherry volume
Ctr.
Zeo200
Zeo500
n= 879
n= 300
n= 451
S

Figure 4

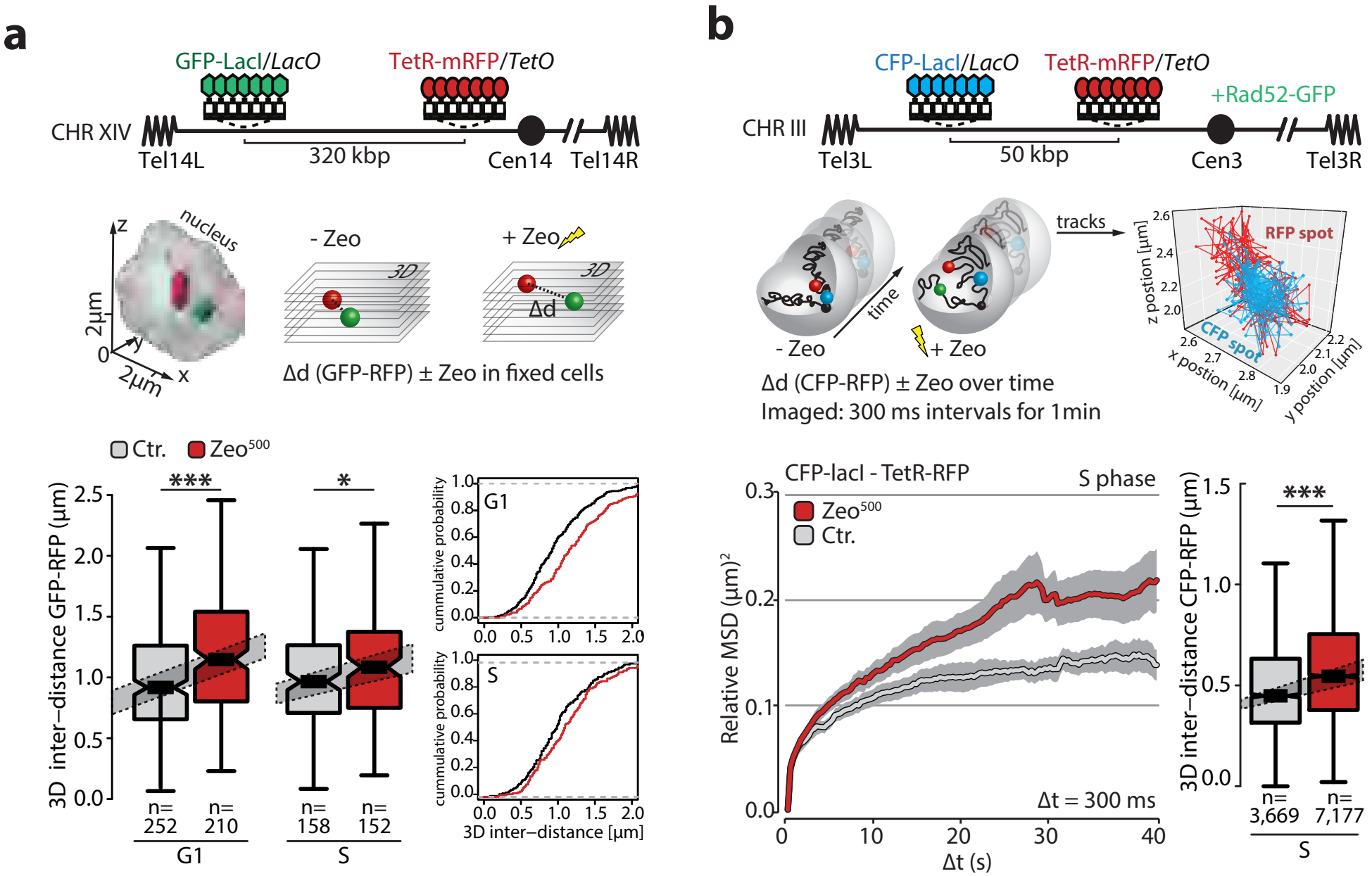
a
GFP-LacI/LacO
TetR-mRFP/TetO
CHR XIV
Tel14L
320 kbp
Cen14
Tel14R
nucleus
z
y
x
2µm
2µm
0
- Zeo
+ Zeo
3D
Δd
Δd (GFP-RFP) ± Zeo in fixed cells
Ctr.
Zeo500
***
*
3D inter–distance GFP-RFP (µm)
n= 252
n= 210
n= 158
n= 152
G1
S
cummulative probability
3D inter–distance [µm]
b
CFP-LacI/LacO
TetR-mRFP/TetO
+Rad52-GFP
CHR III
Tel3L
50 kbp
Cen3
Tel3R
time
- Zeo
+ Zeo
tracks
RFP spot
CFP spot
z postion [µm]
x postion [µm]
y postion [µm]
Δd (CFP-RFP) ± Zeo over time
Imaged: 300 ms intervals for 1min
CFP-lacI - TetR-RFP
S phase
Zeo500
Ctr.
Relative MSD (µm)²
Δt = 300 ms
Δt (s)
3D inter–distance CFP-RFP (µm)
n= 3,669
n= 7,177
S

Figure 5

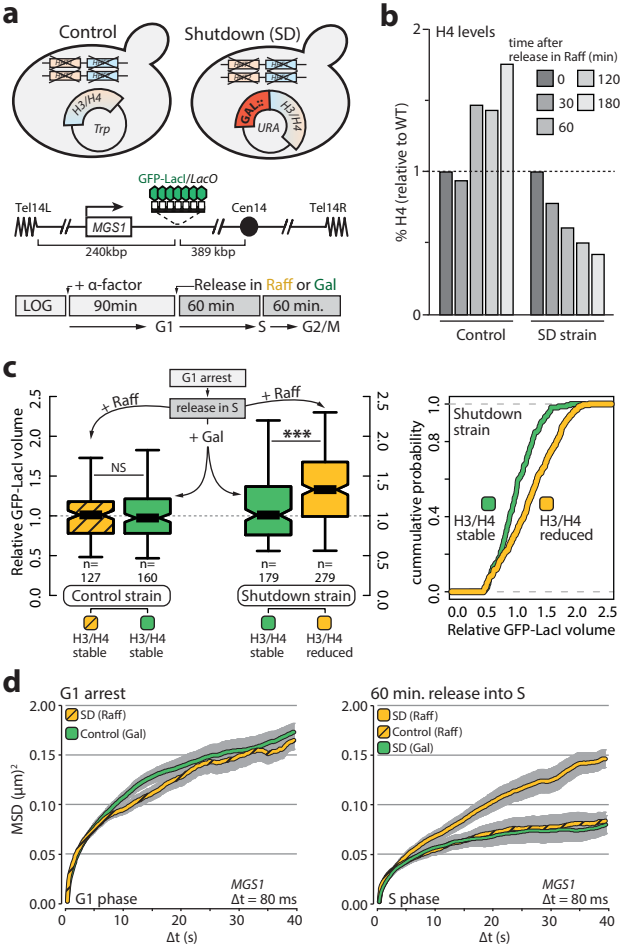
a
Control
Shutdown (SD)
H3/H4
Trp
GAL1
URA
GFP-LacI/LacO
Tel14L
MGS1
Cen14
Tel14R
240kbp
389 kbp
+ α-factor
Release in Raff or Gal
LOG
90min
60 min
60 min.
G1
S
G2/M
b
H4 levels
time after release in Raff (min)
0
30
60
120
180
% H4 (relative to WT)
Control
SD strain
c
G1 arrest
release in S
+ Raff
+ Raff
+ Gal
NS
***
Relative GFP-LacI volume
n= 127
n= 160
n= 179
n= 279
Control strain
Shutdown strain
H3/H4 stable
H3/H4 stable
H3/H4 stable
H3/H4 reduced
Shutdown strain
H3/H4 stable
H3/H4 reduced
cummulative probability
Relative GFP-LacI volume
d
G1 arrest
SD (Raff)
Control (Gal)
MSD (μm)²
G1 phase
MGS1
Δt = 80 ms
Δt (s)
60 min. release into S
SD (Raff)
Control (Raff)
SD (Gal)
S phase
MGS1
Δt = 80 ms
Δt (s)

Figure 6

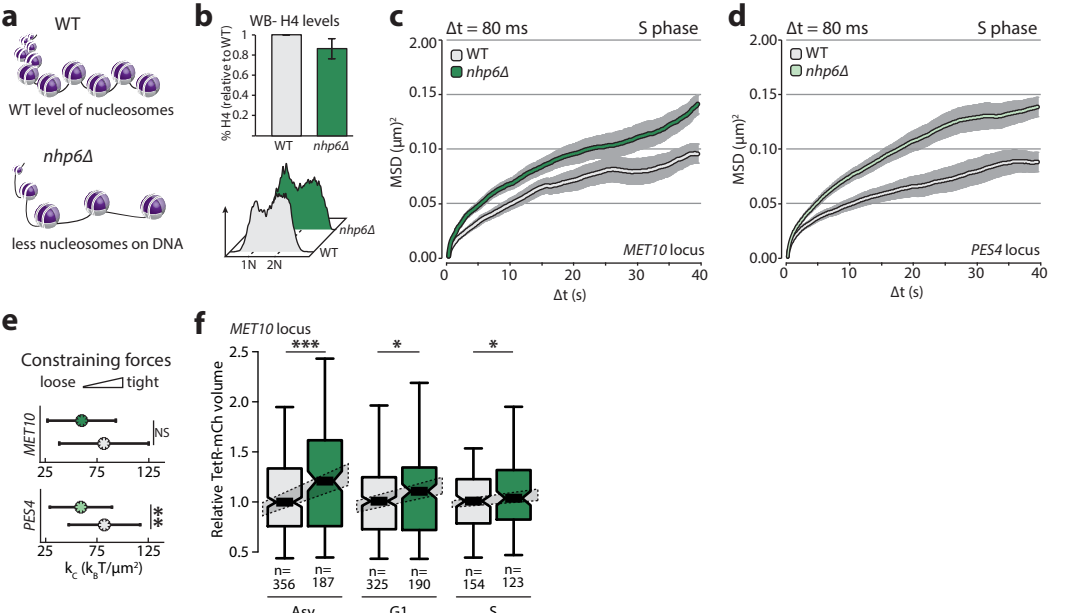
a
WT
WT level of nucleosomes
nhp6Δ
less nucleosomes on DNA
b
WB- H4 levels
% H4 (relative to WT)
1
0.8
0.6
0.4
0.2
WT
nhp6Δ
nhp6Δ
WT
1N
2N
c
Δt = 80 ms
S phase
WT
nhp6Δ
MSD (μm)²
2.00
0.15
0.10
0.05
0.00
0
10
20
30
40
Δt (s)
MET10 locus
d
Δt = 80 ms
S phase
WT
nhp6Δ
MSD (μm)²
2.00
0.15
0.10
0.05
0.00
0
10
20
30
40
Δt (s)
PES4 locus
e
Constraining forces
loose
tight
MET10
NS
25
75
125
PES4
**
25
75
125
k_C (k_BT/μm²)
f
MET10 locus
Relative TetR-mCh volume
2.5
2.0
1.5
1.0
0.5
***
*
*
n= 356
n= 187
n= 325
n= 190
n= 154
n= 123
Asy.
G1
S

Figure 7

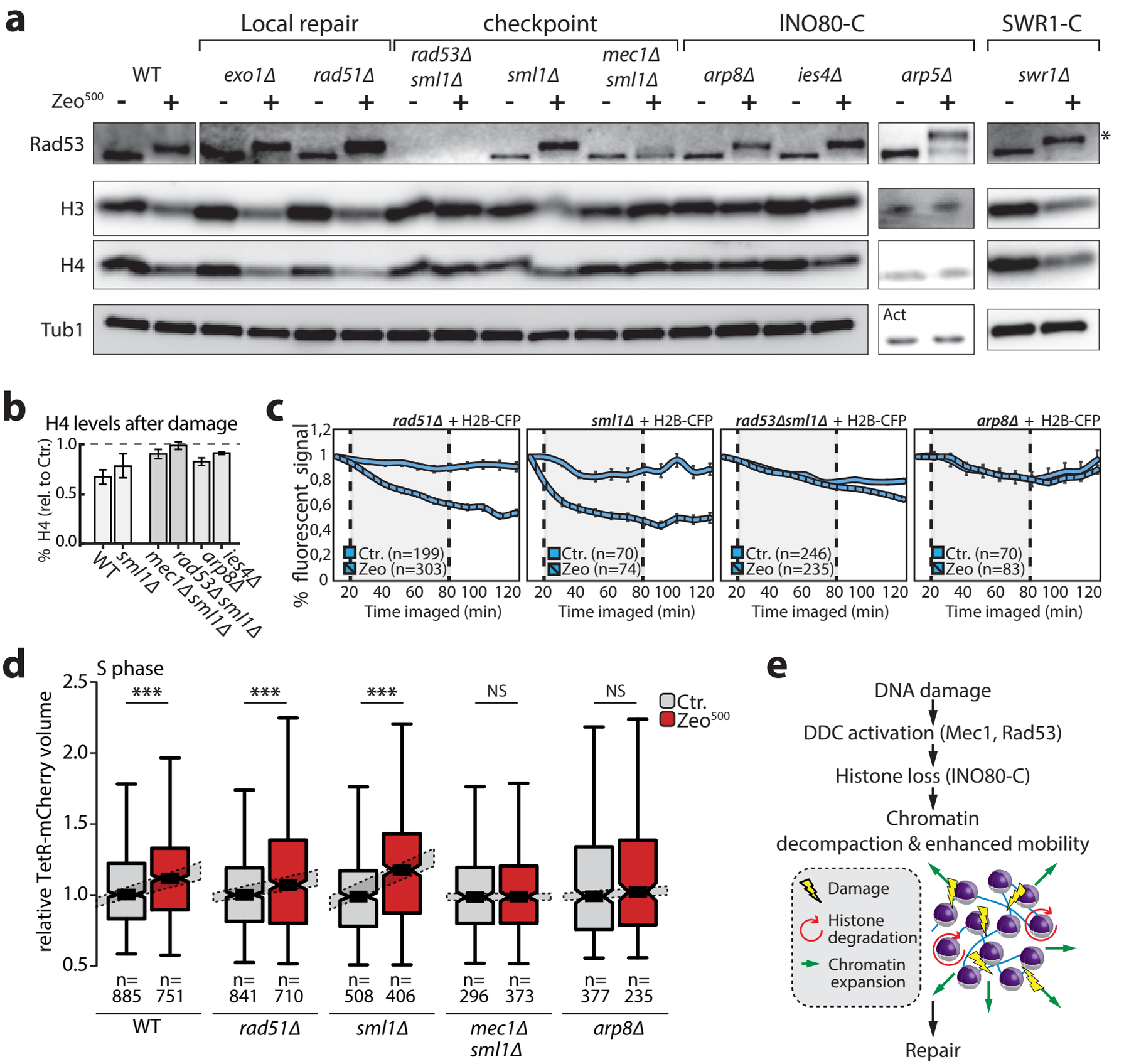
a
Local repair
checkpoint
INO80-C
SWR1-C
WT
exo1Δ
rad51Δ
rad53Δ sml1Δ
sml1Δ
mec1Δ sml1Δ
arp8Δ
ies4Δ
arp5Δ
swr1Δ
Zeo500
Rad53
H3
H4
Tub1
Act
b
H4 levels after damage
% H4 (rel. to Ctr.)
c
rad51Δ + H2B-CFP
sml1Δ + H2B-CFP
rad53Δsml1Δ + H2B-CFP
arp8Δ + H2B-CFP
% fluorescent signal
Ctr. (n=199)
Zeo (n=303)
Ctr. (n=70)
Zeo (n=74)
Ctr. (n=246)
Zeo (n=235)
Ctr. (n=70)
Zeo (n=83)
Time imaged (min)
d
S phase
relative TetR-mCherry volume
Ctr.
Zeo500
***
NS
n= 885
n= 751
n= 841
n= 710
n= 508
n= 406
n= 296
n= 373
n= 377
n= 235
WT
rad51Δ
sml1Δ
mec1Δ sml1Δ
arp8Δ
e
DNA damage
DDC activation (Mec1, Rad53)
Histone loss (INO80-C)
Chromatin decompaction & enhanced mobility
Damage
Histone degradation
Chromatin expansion
Repair

Figure 8

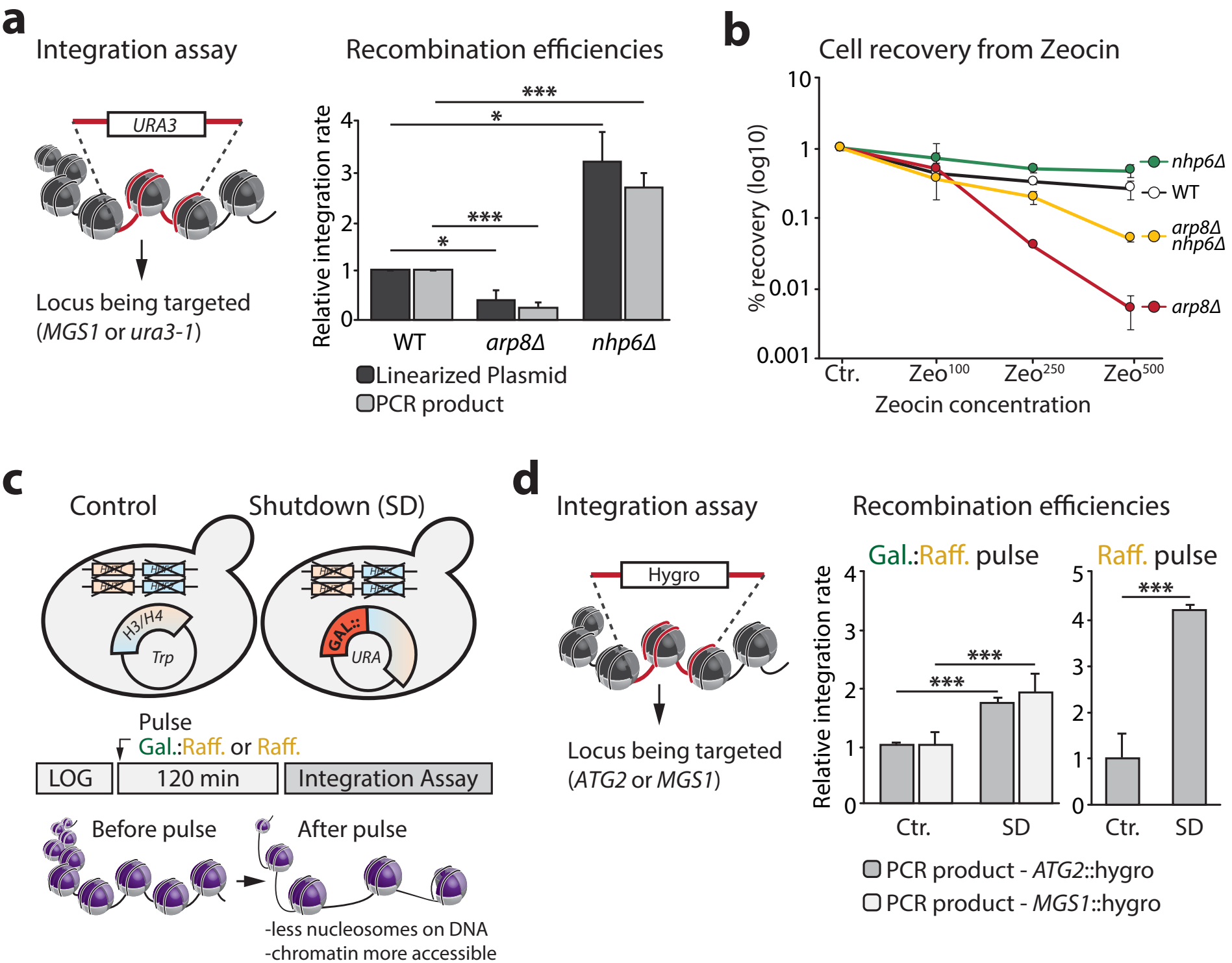
a
Integration assay
URA3
Locus being targeted
(MGS1 or ura3-1)
Recombination efficiencies
Relative integration rate
0
1
2
3
4
***
*
***
*
WT
arp8Δ
nhp6Δ
Linearized Plasmid
PCR product
b
Cell recovery from Zeocin
% recovery (log10)
10
1
0.1
0.01
0.001
Ctr.
Zeo100
Zeo250
Zeo500
Zeocin concentration
nhp6Δ
WT
arp8Δ nhp6Δ
arp8Δ
c
Control
Shutdown (SD)
H3/H4
Trp
GAL::
URA
Pulse
Gal.:Raff. or Raff.
LOG
120 min
Integration Assay
Before pulse
After pulse
-less nucleosomes on DNA
-chromatin more accessible
d
Integration assay
Hygro
Locus being targeted
(ATG2 or MGS1)
Recombination efficiencies
Gal.:Raff. pulse
Raff. pulse
Relative integration rate
0
1
2
3
4
5
***
***
***
Ctr.
SD
Ctr.
SD
PCR product - ATG2::hygro
PCR product - MGS1::hygro

Supplementary Items List

Note that we do NOT copy edit or otherwise change supplementary information, and minor (nonfactual) errors in these documents cannot be corrected after publication.
Please check carefully for errors.

Journal: Nature Structural & Molecular Biology

Article Tracking Number:	NSMB-A36792A
Article Title:	**Histone degradation in response to DNA damage enhances chromatin dynamics and recombination rates**
Corresponding Author:	Susan M. Gasser (Susan.gasser@fmi.ch)

Supplementary items submitted in combined files	
	Please enter numbers below
Number of Supplementary Figures submitted in Integrated Supplementary Figure template	7
Number of Supplementary Tables submitted in combined PDF file	4
Number of Supplementary Notes submitted in combined PDF file	1

Supplementary items submitted in additional files (e.g., Videos, Data Sets and Excel Tables)	
Please list items, titles and captions below, following the examples shown	
Supplementary Item & Number	**Title and Caption**
Supplementary Video 1	**H2B-CFP intensity decreases in response to DNA damage.** Visualization of data shown in **Fig. 1d**. Exemplary time course of 9 individual cells following H2B-CFP intensities after 60 min (20 min – 80 min time point) treatment with 300 µg/ml Zeocin for a total time of 120 min. Shown is a merge of Brightfield (average intensity projections) and CFP (maximum intensity projection) channels. Time-lapse series (120 min total) of 100 optical slices per stack (200nm intervals) were acquired for 12 time points at 10 min intervals, with each slice being exposed for 10 msec per laser line. Video was generated with Fiji (ImagJ) and is shown at 2 frames per second. Original Δt is shown in the top right corner.
Supplementary Video 2	**CFP-LacI, TetR-mRFP time-course used for live cell 3D inter-distance measurements.** Visualization of data shown in Fig. 4b.

	Exemplary time course of CFP-LacI and TetR-mRFP used for 3D inter-distance measurements in living cells. The fluorescent channels were acquired simultaneously on two different CCD cameras; taking 8 optical slices (200nm thickness) per stack every 300 ms for 2 min, with 10 ms exposure times per slice respectively. Video was generated using the Imaris 8.2.0 software and is shown at 25 frames per second (7.5x faster than the original acquisition speed).
Supplementary Dataset 1	**Uncropped Immunoblot images.** Uncropped blot images used in Fig. 1b, 2a, 2b, 2c and 7a
Supplementary Dataset 2	**Summary of mobility parameters.** Table showing the strains, conditions and mobility parameters.
Supplementary Dataset 3	**KNIME workflow.** File contains the KNIME workflow used for imaging data analysis.
Supplementary Dataset 4	**MS search results peptides table cycling cells label swap.** File contains MaxQuant search results used for quantifications.
Supplementary Dataset 5	**MS search results protein groups table cycling cells label swap.** File contains MaxQuant search results used for quantifications.
Supplementary Dataset 6	**MS search results peptides table cycling cells non label swap.** File contains MaxQuant search results used for quantifications.
Supplementary Dataset 7	**MS search results protein groups table cycling cells non label swap.** File contains MaxQuant search results used for quantifications.
Supplementary Dataset 8	**MS search results peptides table G1 arrest cells.** File contains MaxQuant search results used for quantifications.
Supplementary Dataset 9	**MS search results protein groups table G1 arrest cells.** File contains MaxQuant search results used for quantifications.

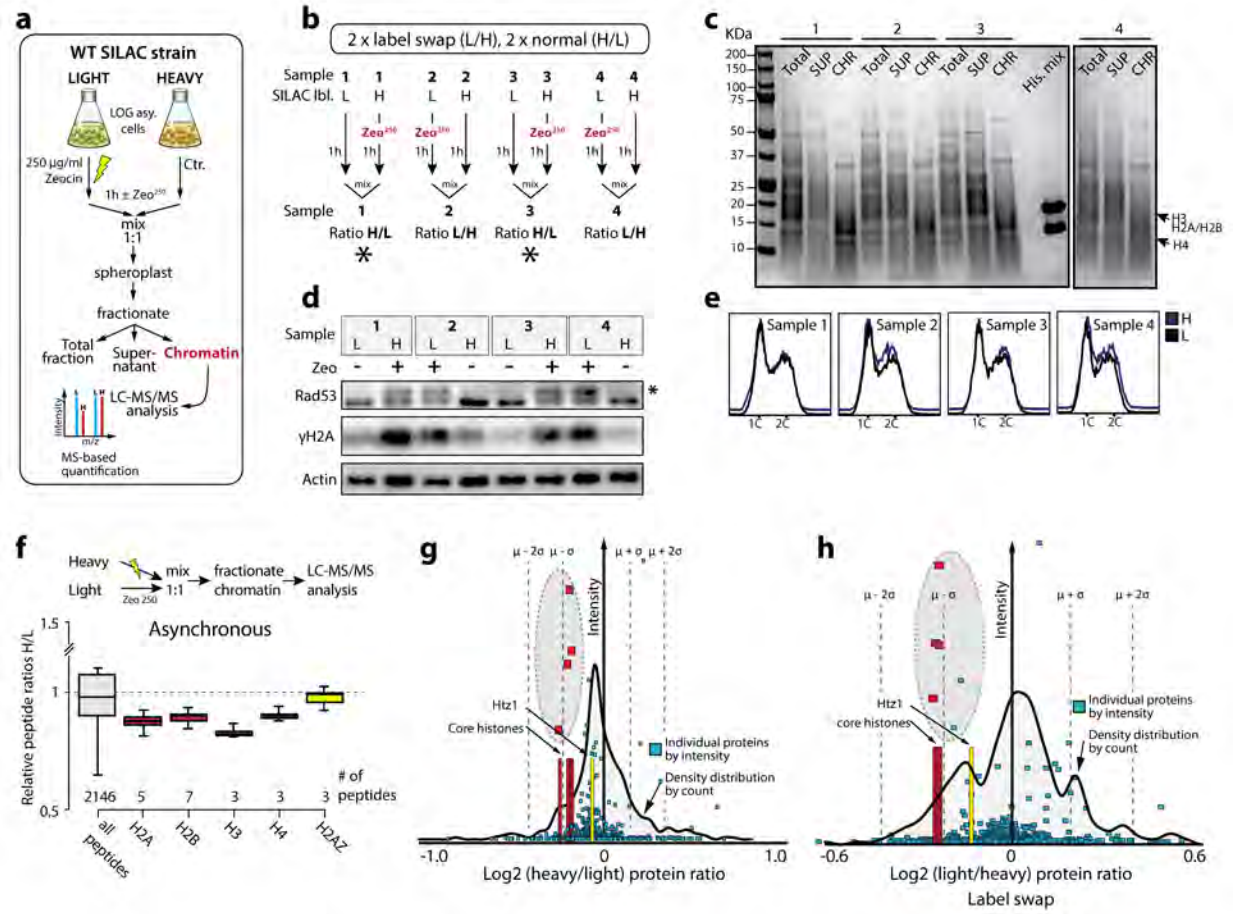

Supplementary Figure 1

SILAC mass spectrometry of pre-enriched chromatin depicts core histone loss

(**a**) Experimental workflow for SILAC mass spectrometry after Zeocin treatment. (**b**) Labeling and mixing of samples from 4 individual experiments. Asterisks indicates label swap (**c**) Colloidal Commassie stained SDS-PAGE of SILAC experiment replicas showing total protein, supernatant (SUP), and chromatin (CHR) fractions from **a**. His. mix is an equimolar mixture of recombinant Histone H2A, H2B, H3 and H4. (**d**) Control Immunoblot analysis using anti-γH2A anti-Rad53 antibodies to show that checkpoint is activated after Zeocin treatment in the SILAC samples from **bc. (e**) FACS analysis showing that all samples from **b-d** have similar cell cycle profiles. Actin was used as loading control. Asterisks indicate the phosphorylation-dependent mobility shift of Rad53. (**f**) SILAC mass spectrometry on chromatin fractions from three independent cell pools. Boxplots show heavy/light histone peptide distribution indicating the degradation of core histones and, to a lesser extent, Htz1 (H2A.Z). (**g**) Distribution of measured protein ratios in the non-label swap experiment or (**h**) label swap experiment. Core histones are labelled red and reside within the μ-σ range. Htz1 is labelled yellow resides closer to the mean ratio of all proteins. Boxplots in **f** represent median values, interquartile ranges and whiskers.

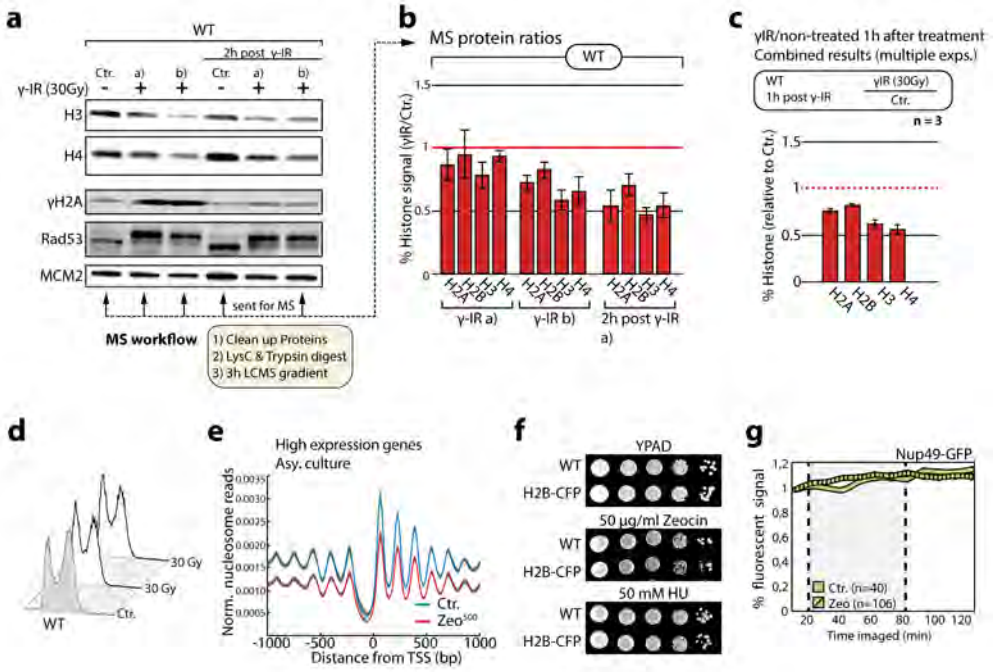

Supplementary Figure 2

Gamma radiation triggers degradation of core histones. Zeocin reduces nucleosome occupancy. H2B-CFP tagging does not interfere with cell viability

(**a**) Immunoblot analysis from one experiment using H3 and H4 specific antibodies on whole cell extracts of asynchronous WT cells exposed to 30 Gy gamma irradiation (γ-IR). Rad53 and γH2A were probed to confirm checkpoint activation. MCM2 was used to control for loading. Arrows indicate samples sent for label-free quantitative mass spectrometric analysis. (**b)** Label-free quantitative mass spectrometry results of samples depicted in **a**. Bar graphs show mean peptide ratios ± s.e.m for the indicated histone proteins upon γIR exposure relative to the control condition. (**c**) Combined label-free mass spectrometry results of sample γ-IR a), γIR b) and an additional experiment. Bar graphs represent the mean peptide ratios (γIR/Ctr.) ± s.e.m. for core histones over all samples. (**d**) FACS analysis showing that all samples have similar cell cycle profiles. (**e**) Genome-wide nucleosome mapping graph shows the distribution of nucleosome reads over 750 highly expressed genes aligned to their TSS from four independent experiments (±s.d. is shaded). (**f**) Drop assay control showing that the H3-CFP fusion complements the absence of H3 in response to genotoxic agents. (**g**) Live single-cell microscopy of Nup49-GFP. Graph shows the the mean fluorescent signals of of all individual cells (cell numbers indicated in graph) per treatment over time relative to the control (Ctr.) condition.

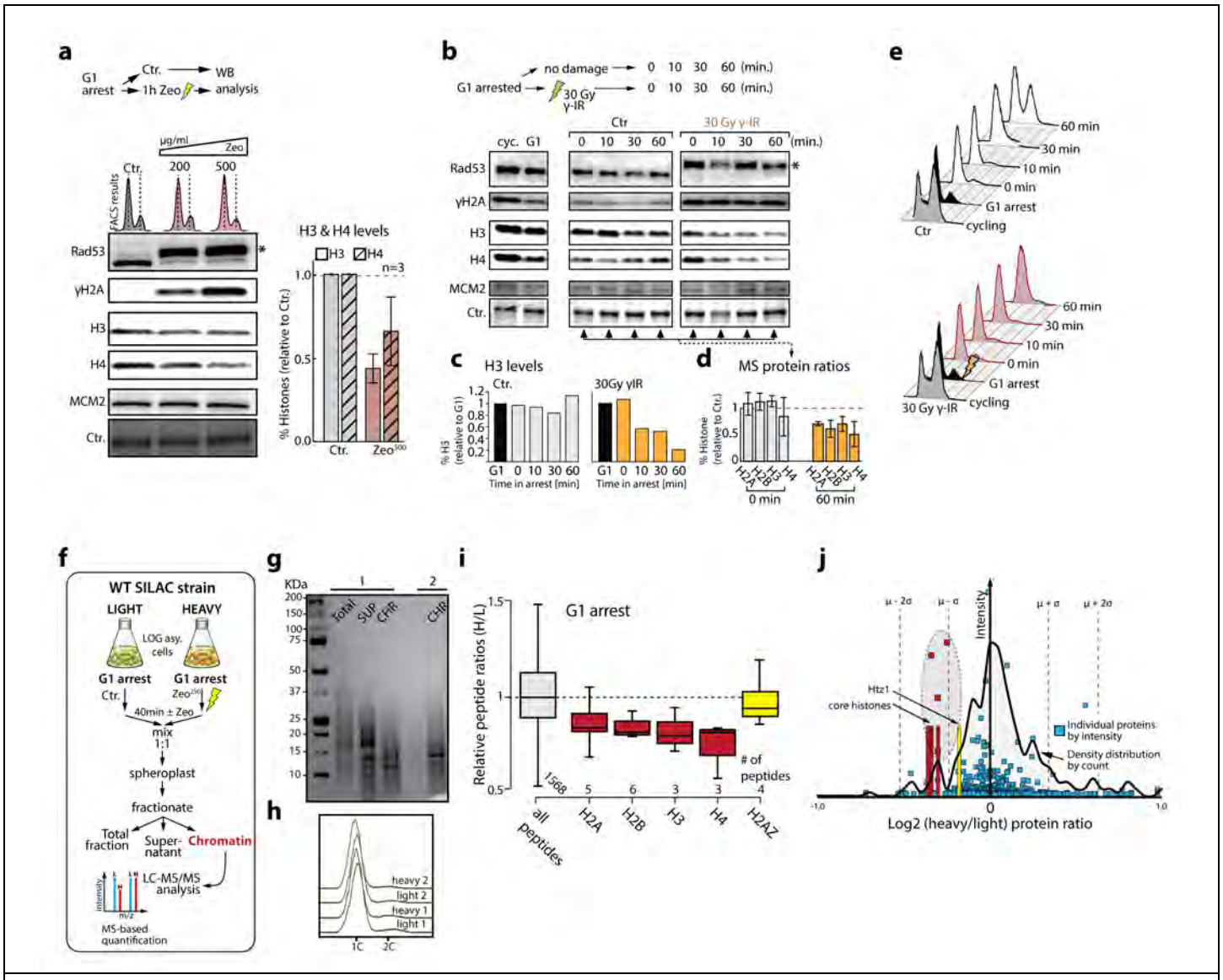

Supplementary Figure 3

Damage-induced histone loss occurs in G1 phase

(**a-b**) Representative immunoblot analysis of whole cell extracts from G1-arrested cells treated with Zeocin **a** or after exposure to γIR **b**. Histone H3 and H4 levels were probed using histone specific antibodies. Rad53 and γH2A were probed to confirm checkpoint activation. MCM2 was used to control for loading and Ctr. represents bands on the ponceau stained membrane. Bar graphs in **a** show the mean ± s.e.m. over three independent replicates relative to the control condition. FACS results of Zeocin treated samples are shown above immunoblots in **a**. Arrows in **b** indicate samples sent for label-free quantitative mass spectrometric analysis. (**c**) Immunoblot quantifications of irradiated samples from one experiment marked with arrows. (**d**) Label-free quantitative mass spectrometry results of samples depicted with arrows. Bar graphs show mean peptide ratios ± s.e.m. for the indicated histone proteins upon γIR exposure relative to the control condition. (**e**) FACS analysis showing cell cycle profiles of all samples from **b**. (**f**) Experimental workflow for SILAC mass spectrometry of G1 arrested cells after Zeocin treatment. (**g**) Commassie stained SDS-PAGE of samples showing total protein, supernatant (SUP), and chromatin (CHR) fractions. (**h**) FACS analysis showing similar G1 arrest efficiency for all samples. (**i**) SILAC mass spectrometry on chromatin fractions from two independent cells pools. Boxplots show heavy/light histone peptide distribution indicating the degradation of core histones and, to a lesser extent, Htz1 (H2A.Z). (**j**) Distribution of measured proteins ratios. Core histones are labelled red and reside within the μ-σ range. Htz1 (H2A.Z) is labelled yellow and residues closer to the mean ratio of all proteins. Boxplots in **i** represent median values, interquartile ranges and whiskers. Asterisk indicates phosphorylation-dependent Rad53 mobility shift.

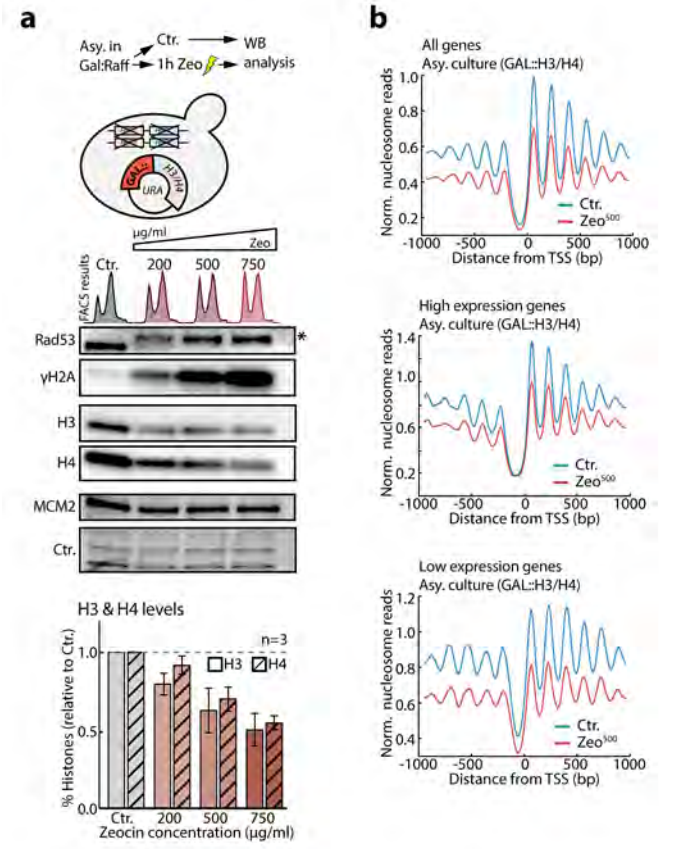

Supplementary Figure 4

Damage-induced histone loss is independent of histone transcription

(**a**) Top panel shows experimental procedure and strain schematic for constitutive histone H3 and H4 transcription in cells grown YPGal:Raff medium. A plasmid borne construct in which the GAL1/10 promoter drives the only pair of histone H3/H4 genes is used. Mid panel shows representative immunoblot analysis using anti-H3 and anti-H4 antibodies on whole cell extracts from the strain depicted in **a** after Zeocin treatment and growth in YPGal:Raff medium. Rad53 and γH2A were probed to confirm checkpoint activation. MCM2 was used to control for loading and Ctr. represents bands on the original gel (UV-TGX stained). Bar graphs in bottom panel show the mean ± s.e.m. over three independent replicates relative to the control condition. Asterisk indicates phosphorylation-dependent Rad53 mobility shift. (**b**) Zeocin treatment causes a genome-wide decrease in nucleosome occupancies. Data represents nucleosome occupancies over the total pool of 5014 protein coding genes, 750 high expression genes and 750 low expression genes aligned to their transcriptional start site (TSS) from one experiment using the strain depicted in **a**.

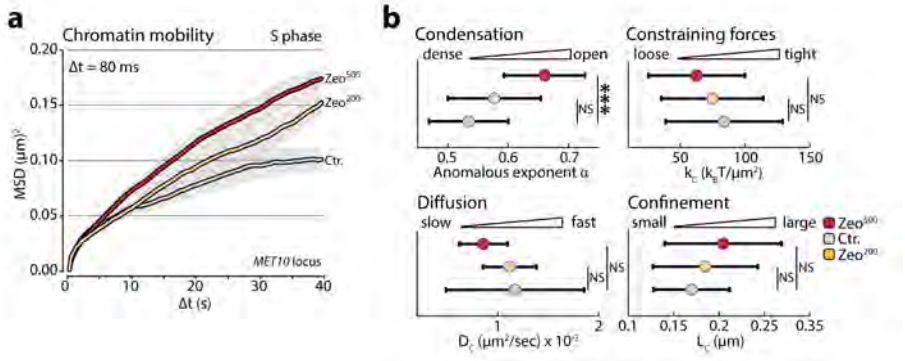

Supplementary Figure 5

High-speed, live cell imaging reveals increase in chromatin movement and loss of constraining forces following DNA damage

(**a**) High-speed (Δt=80 ms) imaging of the undamaged *MET10* locus (as in **Fig. 3a-b**) showing that chromatin mobility increases with Zeocin concentration. Average MSD graphs indicate dose-dependent increases in global chromatin mobility in response to DNA damage ($n^{Ctr.}$=39, n^{Zeo200}=31, n^{Zeo500}=29 different cells from three independent experiments). (**b)** Graphs show the medians and whiskers of biophysical parameters derived from imaging data and predict chromatin decompaction after Zeocin treatment. P-values, ***P<0.001, NS=not significant, result from Kolmogorow-Smirnow-tests. All MSD graphs represent the mean ± s.e.m. of cells pooled from three independent experiments. Additionally, consult Supplementary Dataset 2 for mobility parameters and the number of cells analyzed.

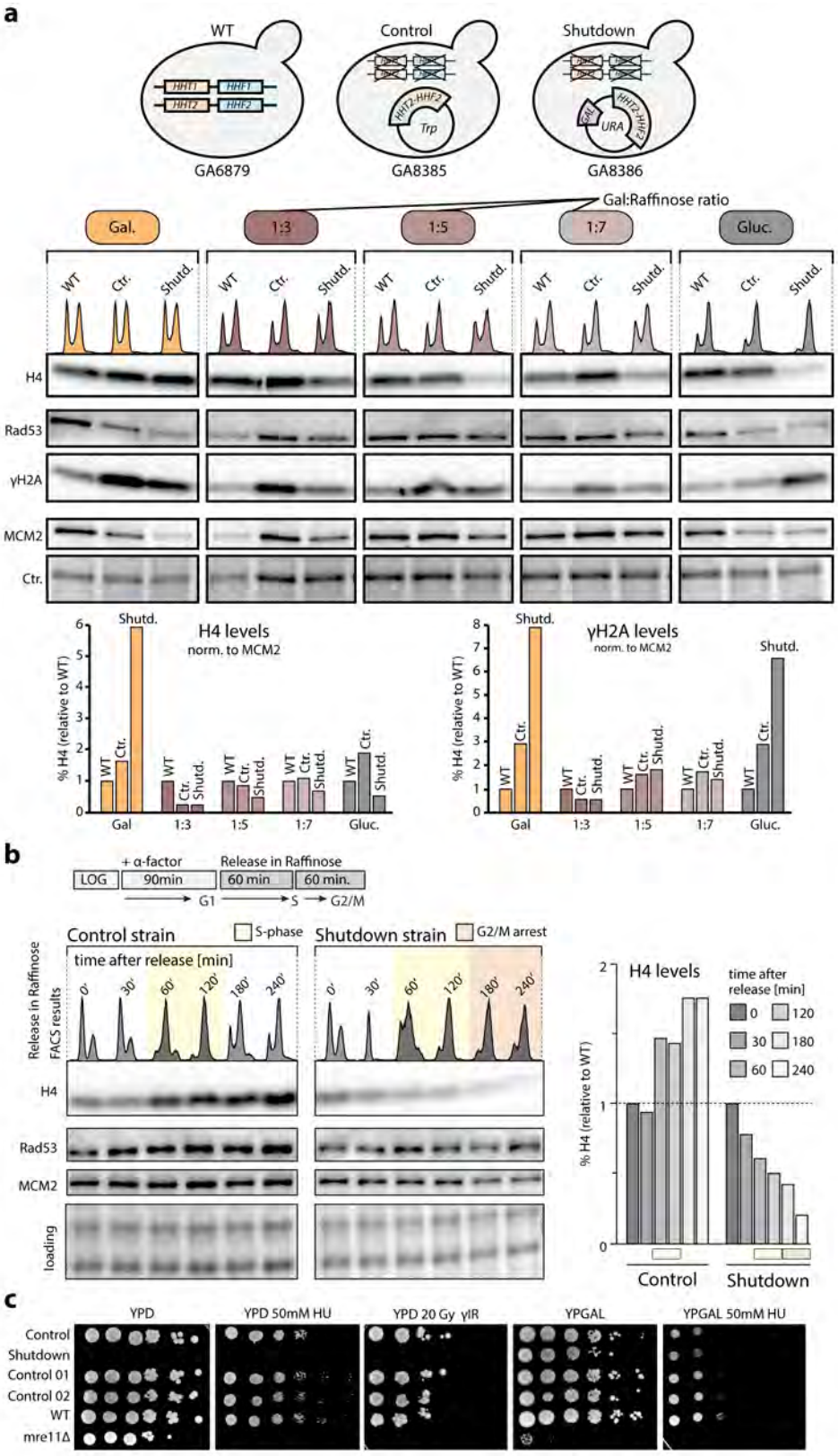
a
WT
Control
Shutdown
HHT1
HHF1
HHT2
HHF2
Trp
URA
GA6879
GA8385
GA8386
Gal:Raffinose ratio
Gal.
1:3
1:5
1:7
Gluc.
WT
Ctr.
Shutd.
H4
Rad53
γH2A
MCM2
Ctr.
H4 levels
norm. to MCM2
% H4 (relative to WT)
γH2A levels
norm. to MCM2
b
+ α-factor
Release in Raffinose
LOG
90min
60 min
60 min.
G1
S
G2/M
Control strain
S-phase
Shutdown strain
G2/M arrest
time after release [min]
0'
30'
60'
120'
180'
240'
Release in Raffinose
FACS results
H4
Rad53
MCM2
loading
H4 levels
time after release [min]
0
30
60
120
180
240
% H4 (relative to WT)
Control
Shutdown
c
YPD
YPD 50mM HU
YPD 20 Gy γIR
YPGAL
YPGAL 50mM HU
Control
Shutdown
Control 01
Control 02
WT
mre11Δ

Supplementary Figure 6
GAL::H3/H4 strain as a tool for *in-vivo* artificially controlled histone level reductions
(**a**) Schematic representation of wild-type, control and shutdown strains grown in the indicated media. Gal. = galactose, gluc. = glucose. Immunoblot analysis of whole cell extracts of the indicated conditions and strains were performed using an antibody directed against Histone H4. Rad53 and γH2A were probed to confirm checkpoint activation. MCM2 was used to control for loading. Bar graphs from quantified immunoblot derived from one experiment shows overexpression or reduction of H3/H4 in the shutdown strain grown in gal. or gluc. medium respectively. Growth of the shutdown strain in Gal:Raff 1:5 confers H3/H4 levels similar to WT. (**b**) Experimental workflow of the arrest-release experiment used to reduce histone levels in S phase (as in **Fig. 5**). Bar graphs from quantified immunoblot data derived from one experiment shows reductions of H3 and H4 upon release into raffinose medium. (**c**) A defined number of exponentially growing cells (fivefold dilutions) was spotted on different YP or YPD plates containing the indicated dose of hydroxyurea (HU). Cells exposed to 20 Gy γIR were spotted onto YPD plates. Drop assays show functionality of shutdown and control strains. Control = control from **a**, control 1 and 2 = similar to control 1 but expressing HHT2-HHF2 from a URA plasmid.

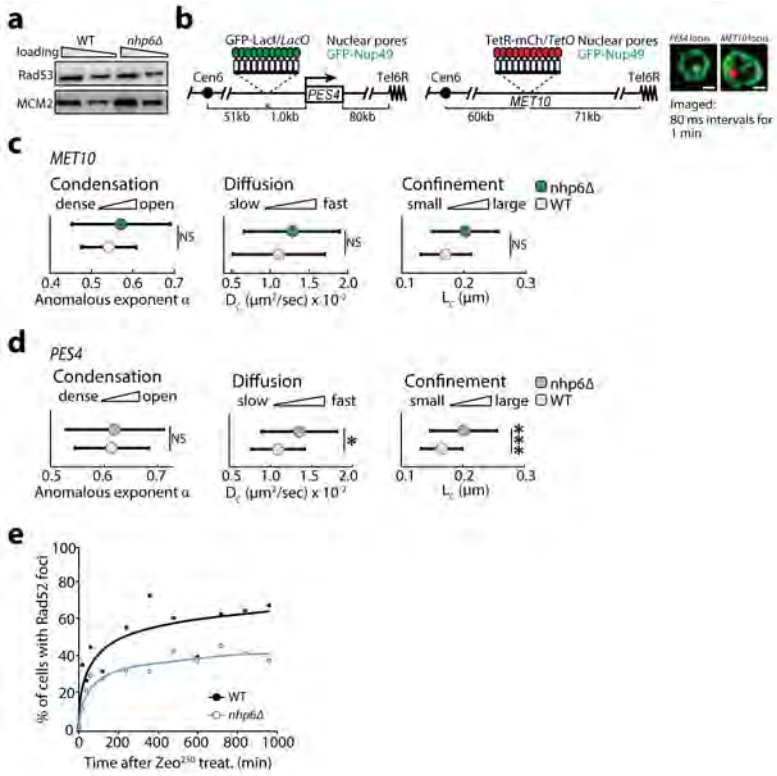

Supplementary Figure 7

Biophysical parameters of *nhp6*Δ tracking data and results from Rad52-YFP recovery assay

(**a**) Control Immunoblot from one experiment (loading 1x and 2x the volume) showing that *nhp6Δ* strains do not have constitutive checkpoint activation. Rad53 was probed to test for checkpoint activation and MCM2 was used as loading control. (**b**) Schematics of the strains used for imaging the *PES4* and *MET10* loci (**Fig. 6c-e**) with representative images. Scale bar is 2 µm. (**c-d**) Graphs show the medians and whiskers of biophysical parameters derived from imaging data of *PES4* **c** and *MET10* **d** (**Fig. 6c,d**). P-values, P*P<0.05, ***P<0.001, NS=not significant, result from Kolmogorow-Smirnow-Tests. (**e**) Rad52-YFP foci recovery assay. Graph shows the overall percentage of Rad52-YFP foci containing cells for each of the 12 time-points from one experiment plotted against the time and shown together with a logarithmic fit.

X

Supplementary Figure 8

Insert figure title here by deleting or overwriting this text; keep title to a single sentence; use Symbol font for symbols and Greek letters.

Insert figure caption here by deleting or overwriting this text; captions may run to a second page if necessary. To ensure accurate appearance in the published version, please use Symbol font for all symbols and Greek letters.

Supplementary Tables

Nucleosome mapping sequencing reads

Supplementary Table 1: Information on sequencing reads obtained for each nucleosome mapping replicate. The strain column indicates the strains used. GA-6879 is the wild type and GA-8386 the shutdown strain grown in galactose:raffinose medium. A-C in the strain column indicates the four independent experiments with or without Zeocin treatment for 1h prior to MNase digestion. Column A shows the *S. Cerevisiae* reads and column B the reads from the *C. glabrata* spike-in control.

	A	**B**	**C=(A+B)**	**E=(A/C)**	**F=(B/C)*100**
Strain	***S. ce.***	***C. glab.***	**total**	**Read fraction *S. cer.***	**Read fraction *C. glab.***
GA-6879_A	50692473.00	9866228.00	60558701.00	0.84	0.16
GA-6879_A_Zeocin	46090144.00	13483686.00	59573830.00	0.77	0.23
GA-6879_B	38787017.00	7282715.00	46069732.00	0.84	0.16
GA-6879_B_Zeocin	36619974.00	10714730.00	47334704.00	0.77	0.23
GA-6879_C	34427922.00	6626795.00	41054717.00	0.84	0.16
GA-6879_C_Zeocin	29746798.00	7722737.00	37469535.00	0.79	0.21
GA-6879_D	25931187.00	4679458.00	30610645.00	0.85	0.15
GA-6879_D_Zeocin	43185379.00	12185328.00	55370707.00	0.78	0.22
GA-8386_A	82089867.00	21788485.00	103878352.00	0.79	0.21
GA-8386_A_Zeocin	53677477.00	20342128.00	74019605.00	0.73	0.27
GA-8386_B	41546073.00	9859227.00	51405300.00	0.81	0.19
GA-8386_B_Zeocin	32786223.00	12332953.00	45119176.00	0.73	0.27
GA-8386_C	25328106.00	6741373.00	32069479.00	0.79	0.21
GA-8386_C_Zeocin	27560758.00	10640545.00	38201303.00	0.72	0.28
GA-8386_D	30336089.00	7284044.00	37620133.00	0.81	0.19
GA-8386_D_Zeocin	31958581.00	12219914.00	44178495.00	0.72	0.28

Yeast strains used in this study

Supplementary Table 2: Yeast strains used in this study. All strains are haploid and all except the SILAC strain and the Htz1-mEos imaging control are derived from the W303 background.

Strain number	Genotype	Source
BY	*MAT**a***; *his3del200*; *leu2del0*; *met15del0*; *trp1del63*; *ura3del0*; (BY4733)	exemplary genotype
W303	*MAT**a***; *ade2-1*; *trp1-1*; *his3-11*; *his3-15*; *ura3-1*; *leu2-3*; *leu2-112*; (W303)	exemplary genotype
JKM179	*MAT**α***; *hml::ADE1*; *hmr::ADE1*; *ade3::GALHO*; *leu2-3*; *lys5 trp1::hisG*; *ura3-52* (JKM179)	exemplary genotype
yAG-06A	*YHR018c::kanMX4*; *YIR034c::kanMX4* (BY4733)	[1]
GA-6879	*MAT**a**, RAD52-YFP*; *NUP49-GFP*; *ADE2::TetR-mCherry*; *lys5::LacI-CFP::TRP*; *leu2::LoxP*; *ZWF1:cutsite(Lmn::lys5::IsceIcs::LEU2::LacO array::Lmn)*; *met10::lmn adaptamers::HIS3::TetOps-LexA* (W303)	[2]
GA-9773	*MAT**a***; *PES4::4xLexA-lacO::TRP1*; *his3-15::GFP-LacI-HIS3*; *NUP49-GFP*	This study
GA-9774	*nhp6a::kanMX4*; *nhp6b::kanMX4*, same as GA-9773	This study
GA-9771	*nhp6a::kanMX4*; *nhp6b::kanMX4*, same as GA-6879	This study
GA-9815	*arp8::NAT,* same as GA9771	
GA-9772	Isogenic to GA-6879	This study
GA-7553	*sml1::HIS3*; same as GA-6879	This study
GA-8132	arp8::NAT; same as GA-6879	This study
GA-8182	ies4::NAT; same as GA-6879	This study
GA-8185	swr1::NAT; same as GA-6879	This study
GA-8202	arp5::NAT; same as GA-6879	This study
GA-7551	*rad51::NAT*; in GA-6879	This study
GA-7552	*rad53::NAT*; same as GA-7553	This study
GA-7556	*mec1::NAT*; same as GA-7553	This study
GA-8385	*MAT**a***; *Nup49-GFP*; *GFP-LacI::HIS3*; *hht2-hhf2Δ hht1-hhf1Δ(no marker) + [#3495 pDM18 pRS415*; *HHT2-HHF2*; *CEN/ARS, TRP1]* (W303)	This study
GA-8386	*MAT**a***; *Nup49-GFP*; *GFP-LacI::HIS3*; *hht2-hhf2Δ hht1-hhf1Δ(no marker) + [#3484 pRM102 pUK420*; *GAL10-HHT2 GAL1-HHF2*; *CEN/ARS, URA3]* (W303)	This study
GA-8387	*MAT**a***; *Nup49-GFP*; *GFP-LacI::HIS3*; *hht2-hhf2Δ hht1-hhf1Δ(no marker) + [#3494 pDM9 pRS416*; *HHT1-HHF1*; *CEN/ARS*; *URA3]* (W303)	This study
GA-9775	*LacO::LEU2::MGS1*, same as GA8385	This study
GA-9776	*LacO::LEU2::MGS1*, same as GA8386	This study
GA-3364	*MAT**a***; *HTB2-CFP::kanXM* (W303)	Brian Luke
GA-9700	*rad51::URA3*; same as GA-3364	This study
GA-9698	*sml1::URA3*; same as GA-3364	This study
GA-9695	*arp8::natMX*; same as GA-3364	This study
GA-9712	*Rad53::natMX*; same as GA-9712	This study
GA-9594	*MAT**α***; *Htz1-Eos::URA3*; same as JKM179	This study
GA-5816	*MAT**α***; *Rad52-YFP*; *NUP49-GFP*; *HIS3::LacI-GFP* (W303)	This study
YMB08 (GA-9227)	*MAT**α***; *ura3-1::LacI-GFP-URA3*; *515kb-XIV::lacO-TRP1*; *YGL117::tetR-mRFP-NATMX*; *196kb-XIV::tetO-LEU2* (W303)	Kerstin Bystricky
GA-9777	*MAT**α***; *YGL117(ARS714)::TetR-mRFP-NAT*; *ade2-1::His3p-CFP-lacI-URA3p-LambdacI-YFP-ADE2*; *leu2-3,112 :: tetO-LEU2*; *74kb :: LambdaO-HIS3*; *40kb :: LacO-TRP1*; *RAD52-EGFP-CaURA3*	This study
GA-1365	*MAT**a**, pre1-1, pre2-2*	[3]
GA-1366	*Mat**a**,* WT strain isogenic to GA-1365 and GA-1366	[3]
GA-1364	*Mat**a**, erg6::LEU2*	[4]

Plasmids used in this study

Supplementary Table 3: Plasmids used in this study

Plasmid number	Description	Type	Yeast selection	Bacterial selection	Source
#3484	pUK420-GAL10-HHT2 GAL1-HHF2	CEN/ARS	URA3	AMP	Addgene [5]
#3494	pRS416-HHT1-HHF1	CEN/ARS	URA3	AMP	[6]
#3495	pRS414-HHT2-HHF2	CEN/ARS	TRP1	AMP	[7]
#279	pRS406	integrating	URA3	AMP	Addgene
#1049	pAG32	see source	see source	see source	[8]
#1050	pAG60	see source	see source	see source	[8]
#2422	pWJ132-hphMX4-Gal1-10	2µ plasmid	ADE2/hphMX4	AMP	This study

Antibodies used in this study

Supplementary Table 4: Antibodies used in this study

Antibody	Supplier	Conditions used
Mouse α Rad53	Custom made antibody (GenScript)	1:200 in milk
Rabbit α H4	Abcam AB 10158	1:5000 or 1:7500 in BSA
Mouse α actin	MAB1501	1:10,000 in milk
Goat α MCM2	Santa Cruz (SC 6680)	1:3000 in BSA
Rabbit α γH2A	Custom made antibody	1:3000 i BSA
Rabbit α H3	Abcam AB1791	1:10,000 in BSA
Rabbit α Ubiquitin	Abcam (AB19247)	1:2000 in milk

Supplementary Table References

1. Gruhler, A. et al. Quantitative phosphoproteomics applied to the yeast pheromone signaling pathway. *Mol Cell Proteomics* **4**, 310-27 (2005).
2. Seeber, A., Dion, V. & Gasser, S.M. Checkpoint kinases and the INO80 nucleosome remodeling complex enhance global chromatin mobility in response to DNA damage. *Genes Dev* **27**, 1999-2008 (2013).
3. Richterruoff, B., Wolf, D.H. & Hochstrasser, M. Degradation of the Yeast Mat-Alpha-2 Transcriptional Regulator Is Mediated by the Proteasome. *Febs Letters* **354**, 50-52 (1994).
4. Heese-Peck, A. et al. Multiple functions of sterols in yeast endocytosis. *Mol Biol Cell* **13**, 2664-80 (2002).
5. Mann, R.K. & Grunstein, M. Histone H3 N-terminal mutations allow hyperactivation of the yeast GAL1 gene in vivo. *EMBO J* **11**, 3297-306 (1992).
6. Duina, A.A. & Winston, F. Analysis of a mutant histone H3 that perturbs the association of Swi/Snf with chromatin. *Molecular and Cellular Biology* **24**, 561-572 (2004).
7. Park, J.H., Cosgrove, M.S., Youngman, E., Wolberger, C. & Boeke, J.D. A core nucleosome surface crucial for transcriptional silencing. *Nature Genetics* **32**, 273-279 (2002).
8. Goldstein, A.L. & McCusker, J.H. Three new dominant drug resistance cassettes for gene disruption in Saccharomyces cerevisiae. *Yeast* **15**, 1541-1553 (1999).

Supplementary Notes

Estimating the anomalous diffusion exponent α and the diffusion coefficient

We computed the cross-correlation (CC) function using [1]:

$$C(t) = \frac{1}{N_p - t} \sum_{k=1}^{N_p - t} (\mathbf{R}_c(k\Delta t) - \mathbf{R}_c((k+t)\Delta t)^2, \tag{6}$$

for $t = 1, T-1$, where N_p is the number of points in the trajectory. In many studies the CC is referred to as the MSD function [2,3] although these two functions are distinct[1]. The MSD is defined as the squared displacement with respect to the initial trajectory position, averaged over time:

$$\text{MSD(t)} = \left\langle \left(R_c(t) - R_c(0) \right)^2 \right\rangle.$$

For short times, $C(t)$ increases as a power law

$$C(t) = Ct^{\alpha}. \tag{7}$$

where $C > 0$. To extract the coefficient α, we computed $C(t)$ from empirical trajectories and fitted the first seven points of the curve to a power law. A chromatin or DNA locus is characterized experimentally by $\alpha < 1$ [4,5], while for normal diffusion $\alpha = 1$. In the Rouse polymer model[6], the anomalous exponent is $\alpha = 0.5$ computed for intermediate time regime (see [6]).

To compute the diffusion coefficient of the tagged monomer, we use the following empirical estimator described in [1]:

$$D_c = \frac{1}{4\Delta t} \sum_{k=1}^{N_p - 1} (\mathbf{R}_c(k\Delta t) - \mathbf{R}_c((k+1)\Delta t))^2, \tag{8}$$

For short time interval $\Delta t = b^2/D$, the locus motion is Brownian and the diffusion coefficient is well approximated by eq.(8).

Estimating the effective spring coefficient k_c

Because the chromatin interacts locally with its environment, we estimated this interaction using a polymer model[7], by a harmonic well of strength k acting on a single monomer $\mathbf{R}_n$. The potential energy of the interaction is

$$U(\mathbf{R}_n) = \frac{1}{2} k(\mathbf{R}_n - \boldsymbol{\mu})^2, \tag{9}$$

where $\boldsymbol{\mu}$ is the fix position of the interaction. The velocity of an observed monomer c, averaged over many trajectories is driven by this interacting force, following the relation described in [7]:

$$\lim_{\Delta t \to 0} E\{\frac{\mathbf{R}_c(t+\Delta t) - \mathbf{R}_c(t)}{\Delta t} \mid \mathbf{R}_c(t) = \mathbf{x}\} = -Dk_{cn}(\mathbf{x} - \boldsymbol{\mu}), \tag{10}$$

where $\mathbf{R}_c(t)$ is the position of locus c at time t and D the diffusion coefficient and $E\{. \mid \mathbf{R}_c(t) = \mathbf{x}\}$ means averaging over trajectory realizations such that the condition $\mathbf{R}_c(t) = \mathbf{x}$ is satisfied. Relation (18) links the average velocity of the observed monomer c to the force applied at a distance $|c - n|$. For a Rouse polymer, with a potential well of type (17), the effective spring coefficient is given by

$$k_{cn} = \frac{k\kappa}{\kappa + |c - n| k}, \tag{11}$$

where κ is the monomer-monomer spring coefficient. We estimated k_c from the empirical locus trajectories $\mathbf{R}_c(t)$ by

$$k_c \approx \frac{1}{2(N_p - 1)} \sum_{i=1}^{2} \sum_{h=1}^{N_p - 1} \frac{R_c^i((h+1)\Delta t) - R_c^i(h\Delta t)}{D_c \Delta t (R_c^i(h\Delta t) - \langle R_c^i \rangle)}, \tag{12}$$

where i is the spatial direction (in two dimensions, we sum over the x and y components) and N_p is the number of points in the trajectory. In practice, the quantity $\langle R_c^i \rangle$ is computed by averaging over the trajectory. The diffusion coefficient D_c can be computed by using eq. 8.

Supplementary Notes References

1. Schuss, Z. Diffusion and Stochastic Processes. An Analytical Approach. *Springer-Verlag, New York, NY* (2009).
2. Dion, V., Kalck, V., Horigome, C., Towbin, B.D. & Gasser, S.M. Increased mobility of double-strand breaks requires Mec1, Rad9 and the homologous recombination machinery. *Nat Cell Biol* **14**, 502-9 (2012).
3. Mine-Hattab, J. & Rothstein, R. Increased chromosome mobility facilitates homology search during recombination. *Nat Cell Biol* **14**, 510-7 (2012).
4. Kepten, E., Bronshtein, I. & Garini, Y. Improved estimation of anomalous diffusion exponents in single-particle tracking experiments. *Physical Review E* **87**(2013).
5. Weber, S.C., Theriot, J.A. & Spakowitz, A.J. Subdiffusive motion of a polymer composed of subdiffusive monomers. *Phys Rev E Stat Nonlin Soft Matter Phys* **82**, 011913 (2010).
6. Doi, M., Edwards, S. F. The Theory of Polymer Dynamics. . *Oxford: Clarendon Press.* (1986).
7. Amitai, A., Toulouze, M., Dubrana, K. & Holcman, D. Analysis of Single Locus Trajectories for Extracting In Vivo Chromatin Tethering Interactions. *PLoS Computational Biology* **11**, e1004433 (2015).

Fig. 1b

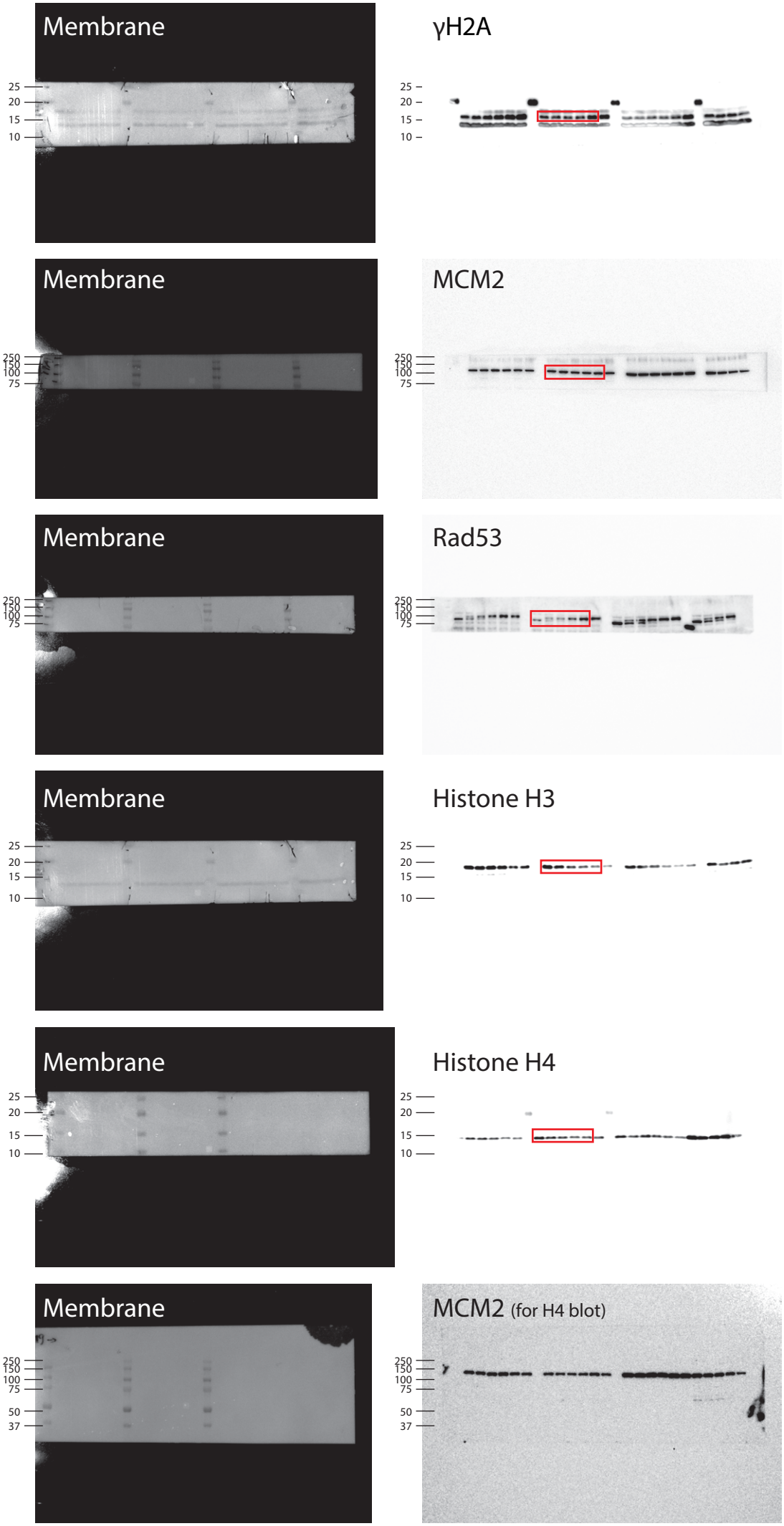
Membrane
25
20
15
10
γH2A
25
20
15
10
Membrane
250
150
100
75
MCM2
250
150
100
75
Membrane
250
150
100
75
Rad53
250
150
100
75
Membrane
25
20
15
10
Histone H3
25
20
15
10
Membrane
25
20
15
10
Histone H4
25
20
15
10
Membrane
250
150
100
75
50
37
MCM2 (for H4 blot)
250
150
100
75
50
37

Fig. 1b

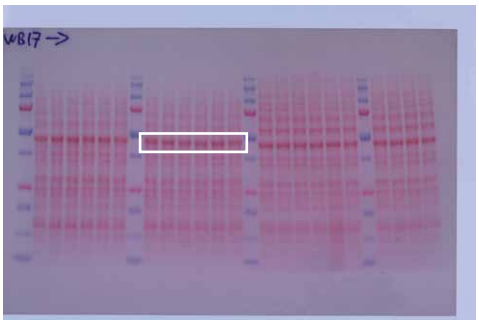

Ponceau stained membrane after transfer

Fig. 2a

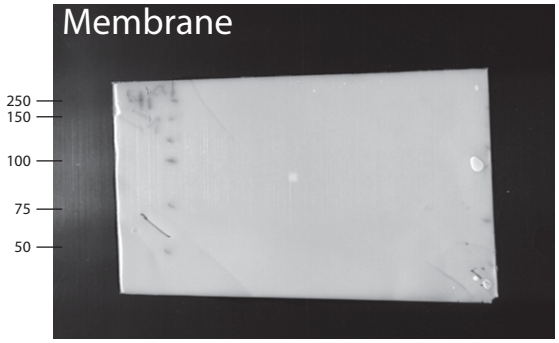
Membrane
250
150
100
75
50

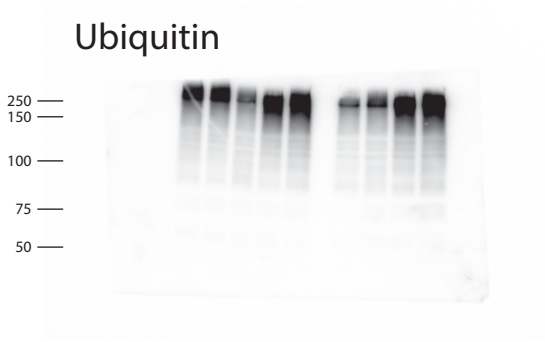
Ubiquitin
250
150
100
75
50

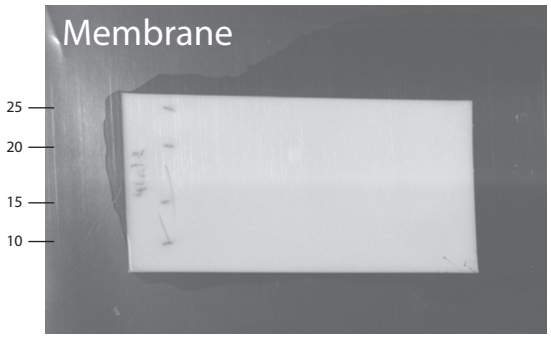
Membrane
25
20
15
10

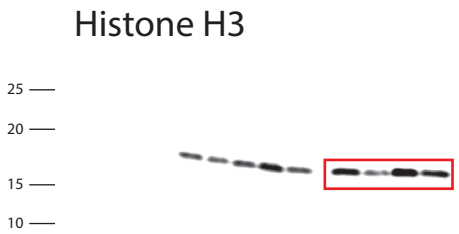
Histone H3
25
20
15
10

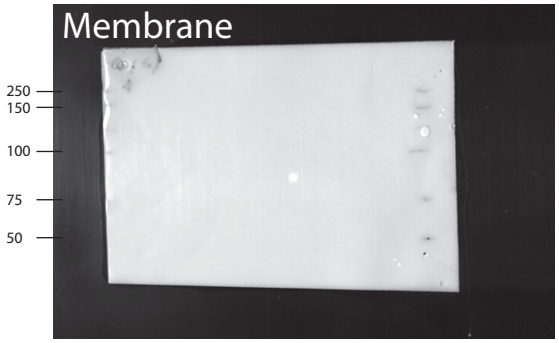
Membrane
250
150
100
75
50

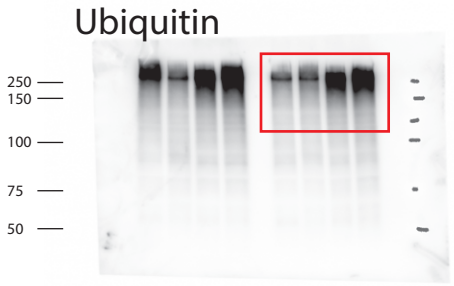
Ubiquitin
250
150
100
75
50

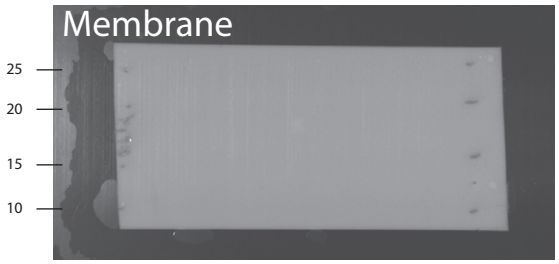
Membrane
25
20
15
10

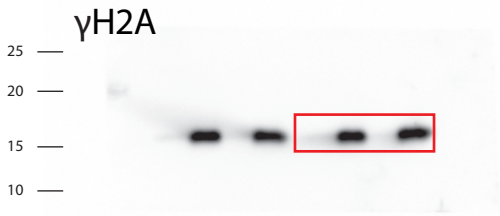
γH2A
25
20
15
10

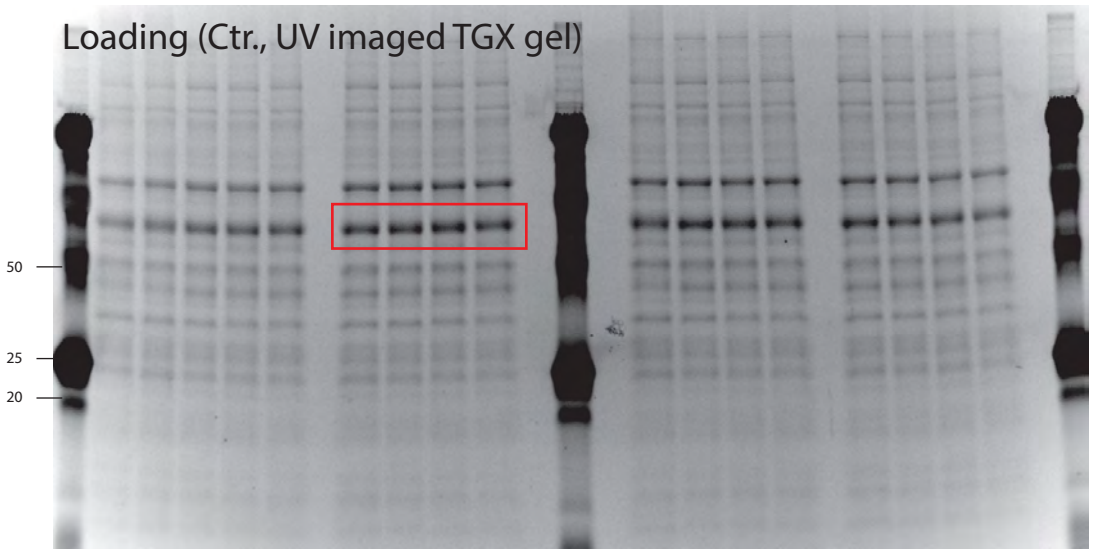
Loading (Ctr., UV imaged TGX gel)
50
25
20

Fig. 2b

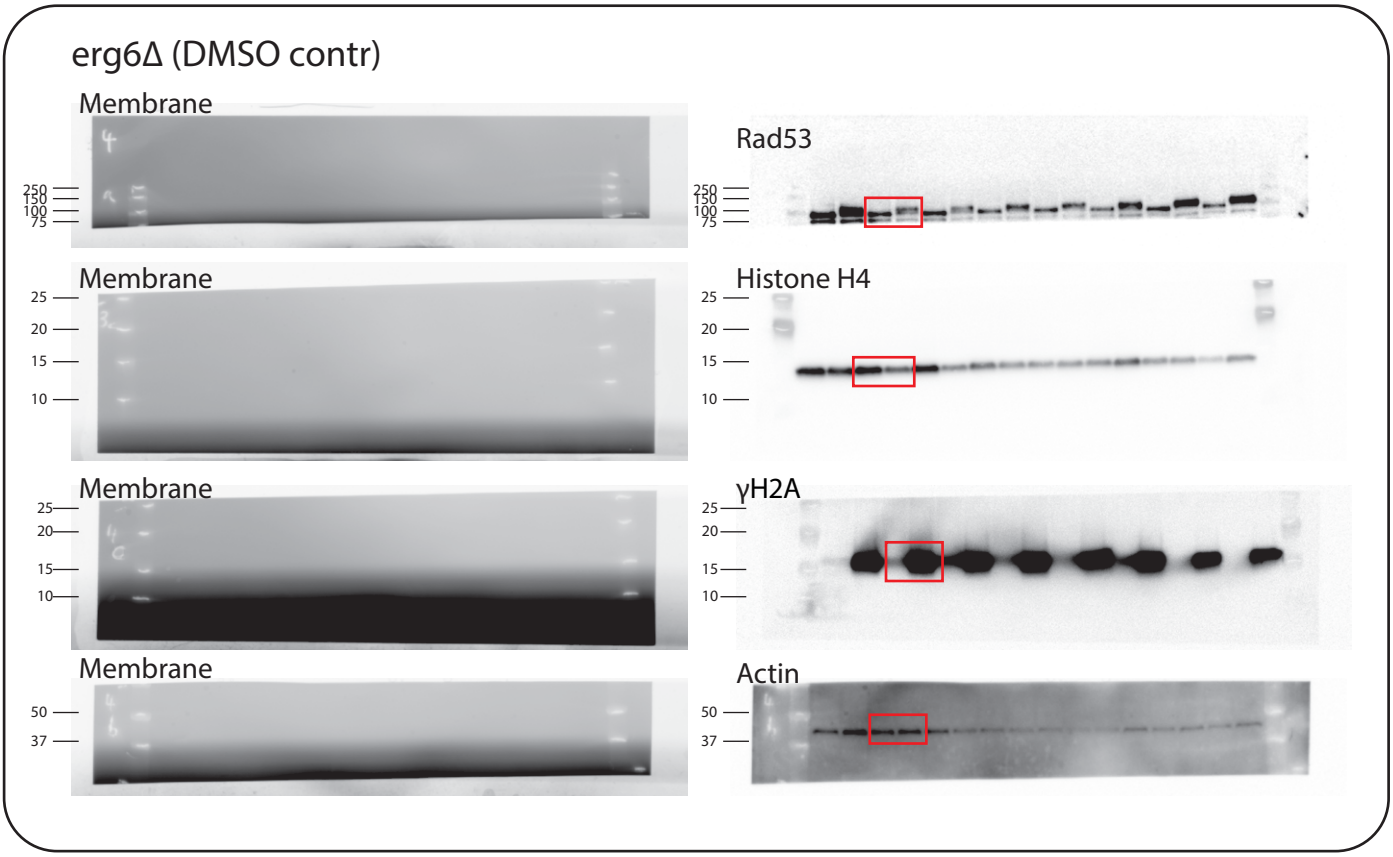
erg6Δ (DMSO contr)
Membrane
250
150
100
75
Rad53
Membrane
25
20
15
10
Histone H4
Membrane
γH2A
Membrane
50
37
Actin

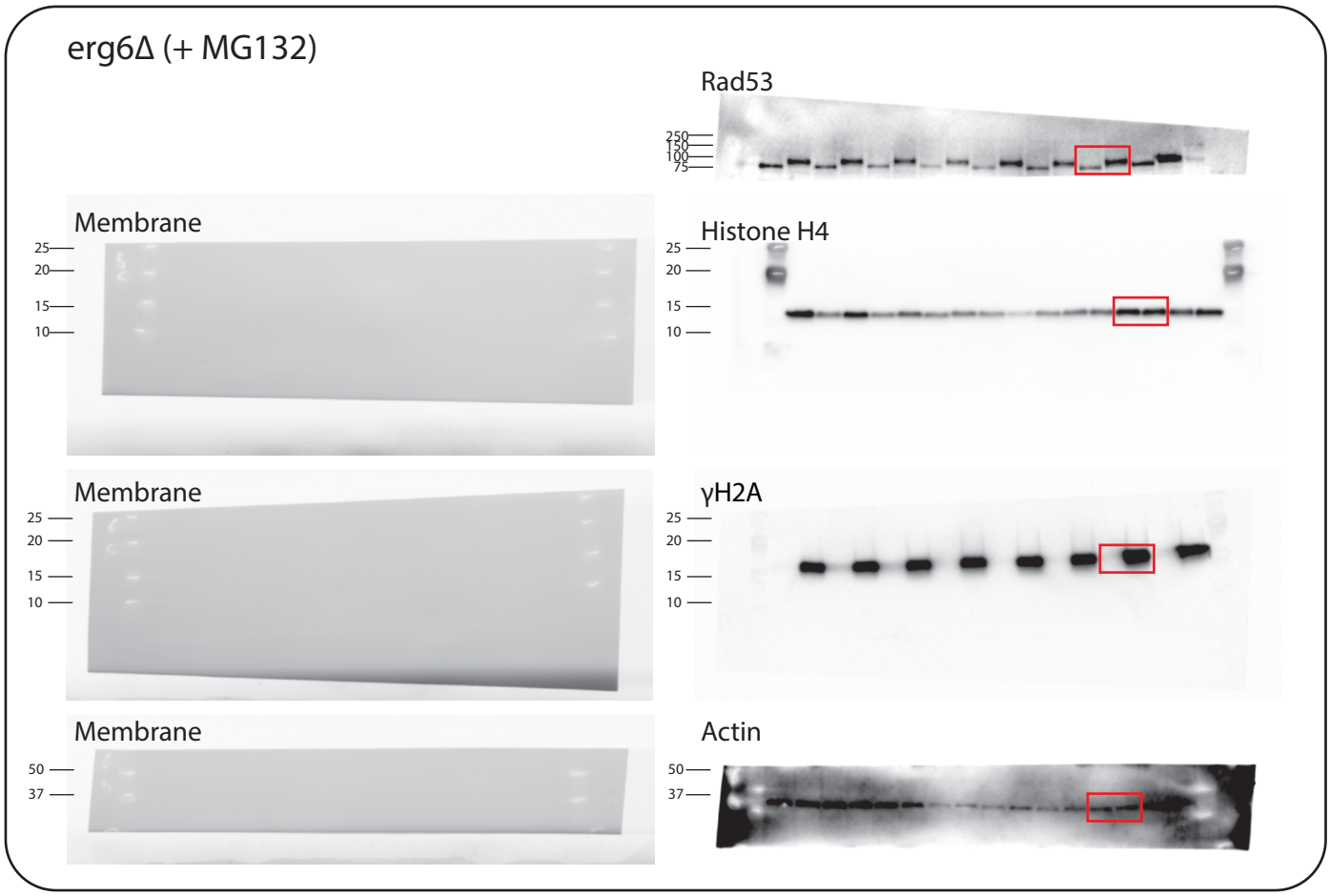
erg6Δ (+ MG132)
Rad53
250
150
100
75
Membrane
25
20
15
10
Histone H4
Membrane
γH2A
Membrane
50
37
Actin

Fig. 2c

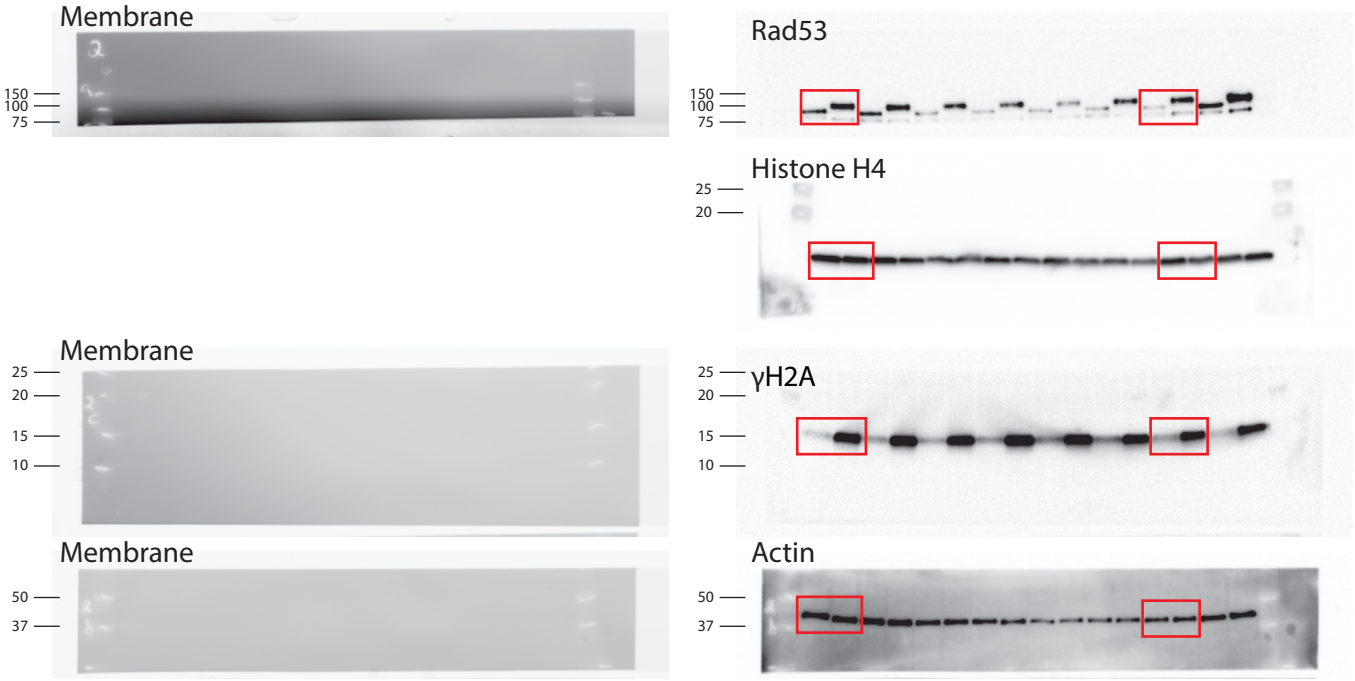
Membrane
150
100
75
Rad53
150
100
75
Histone H4
25
20
Membrane
25
20
15
10
γH2A
25
20
15
10
Membrane
50
37
Actin
50
37

Fig. 7a

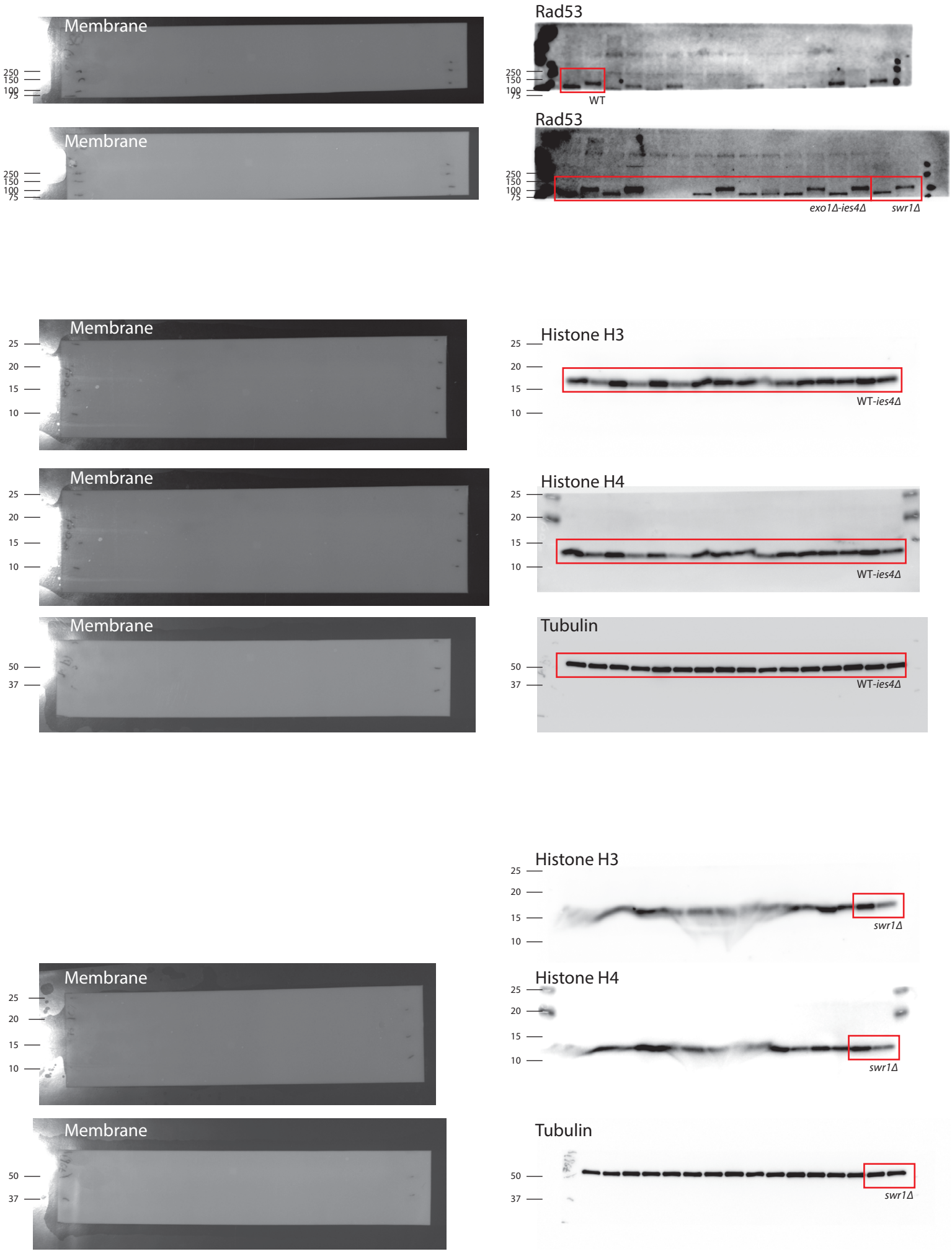
Membrane
250
150
100
75
Rad53
WT
Membrane
Rad53
exo1Δ-ies4Δ
swr1Δ
Membrane
25
20
15
10
Histone H3
WT-ies4Δ
Membrane
Histone H4
WT-ies4Δ
Membrane
50
37
Tubulin
WT-ies4Δ
Histone H3
swr1Δ
Membrane
Histone H4
swr1Δ
Membrane
Tubulin
swr1Δ

Fig. 7a

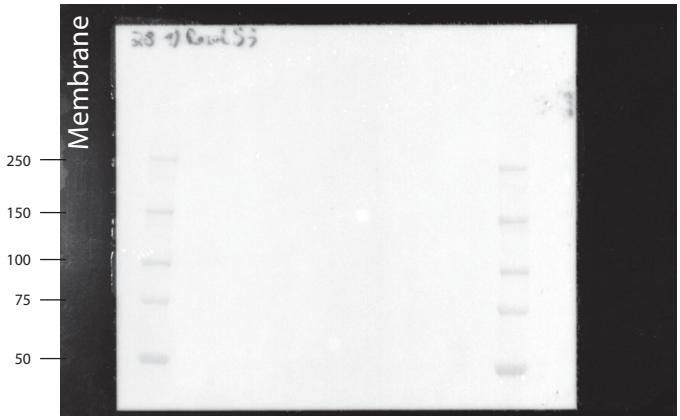

Rad53

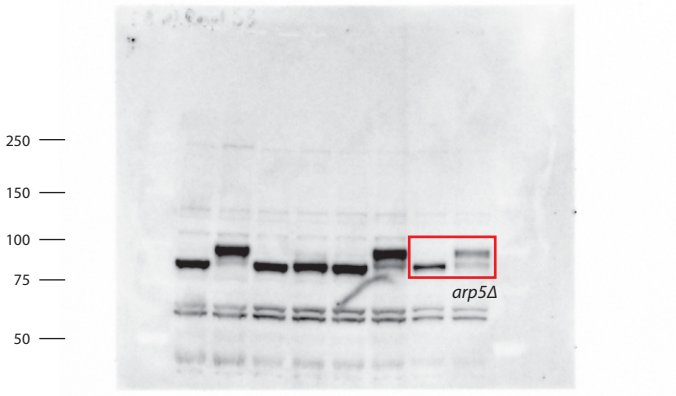

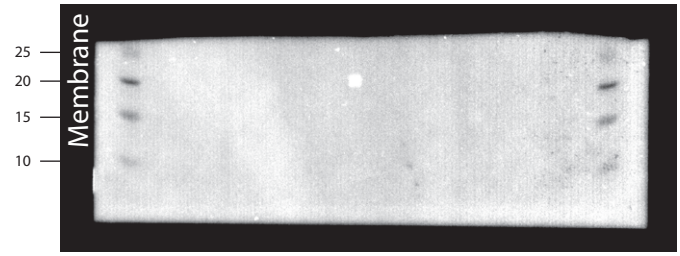

Histone H3

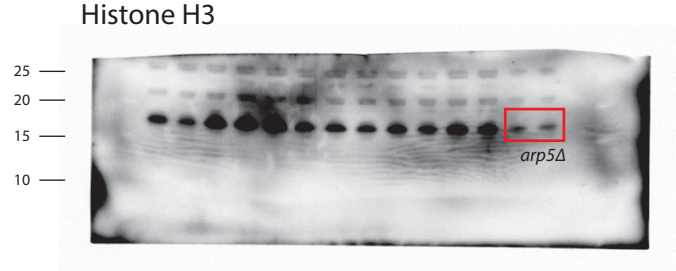

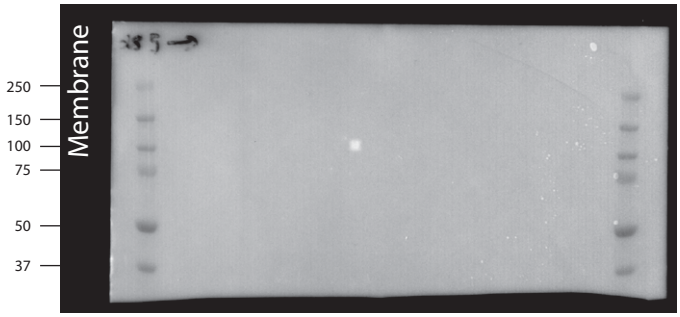

Actin (for H3 blot)

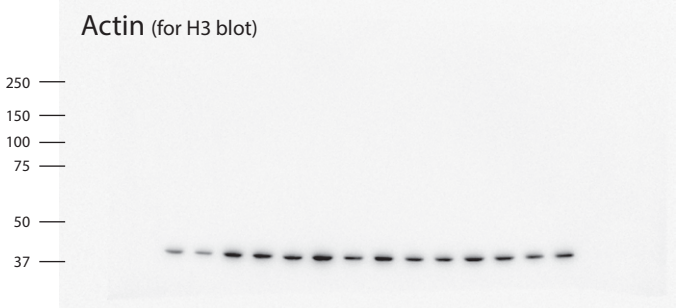

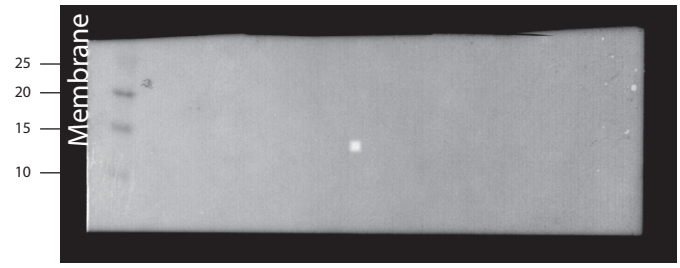

Histone H4

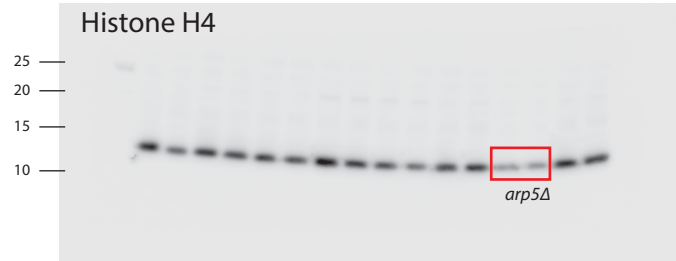

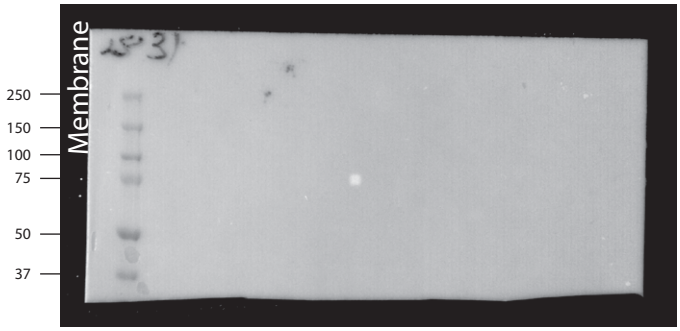

Actin (for H4 blot)